



Does global warming amplify interannual climate variability?

Chao He^{1,2} · Tim Li^{2,3}

Received: 26 December 2017 / Accepted: 28 May 2018 / Published online: 4 June 2018
© Springer-Verlag GmbH Germany, part of Springer Nature 2018

Abstract

Based on the outputs of 30 models from Coupled Model Intercomparison Project Phase 5 (CMIP5), the fractional changes in the amplitude interannual variability (σ) for precipitation (P') and vertical velocity (ω') are assessed, and simple theoretical models are constructed to quantitatively understand the changes in $\sigma(P')$ and $\sigma(\omega')$. Both RCP8.5 and RCP4.5 scenarios show similar results in term of the fractional change per degree of warming, with slightly lower inter-model uncertainty under RCP8.5. Based on the multi-model median, $\sigma(P')$ generally increases but $\sigma(\omega')$ generally decreases under global warming but both are characterized by non-uniform spatial patterns. The $\sigma(P')$ decrease over subtropical subsidence regions but increase elsewhere, with a regional averaged value of $1.4\% \text{ K}^{-1}$ over 20°S – 50°N under RCP8.5. Diagnoses show that the mechanisms for the change in $\sigma(P')$ are different for climatological ascending and descending regions. Over ascending regions, the increase of mean state specific humidity contributes to a general increase of $\sigma(P')$ but the change of $\sigma(\omega')$ dominates its spatial pattern and inter-model uncertainty. But over descending regions, the change of $\sigma(P')$ and its inter-model uncertainty are constrained by the change of mean state precipitation. The $\sigma(\omega')$ is projected to be weakened almost everywhere except over equatorial Pacific, with a regional averaged fractional change of $-3.4\% \text{ K}^{-1}$ at 500 hPa. The overall reduction of $\sigma(\omega')$ results from the increased mean state static stability, while the substantially increased $\sigma(\omega')$ at the mid-upper troposphere over equatorial Pacific and the inter-model uncertainty of the changes in $\sigma(\omega')$ are dominated by the change in the interannual variability of diabatic heating.

Keywords Global warming · Interannual variability · Precipitation · Vertical velocity

1 Introduction

The year-to-year fluctuation of the climate from its mean state is referred to as interannual variability, such as the deviation of precipitation and temperature at interannual time-scale from the mean state. Interannual climate variability

is essential for the occurrence of disastrous climate events, especially wide-spread droughts and floods (e.g., Dai and Wigley 2000; Ding 2007; Li et al. 2013; Stevenson et al. 2015; Zhang and Zhou 2015), such as the great drought in 1994 (Park and Schubert 1997; Guan and Yamagata 2003) and great flood in 1998 over a major fraction of East Asia (Guo et al. 2002; Lee et al. 2004). Interannual climate variability is driven by a variety of factors, including atmospheric internal dynamic, ocean–atmosphere interaction and land–atmosphere interaction (e.g., Wallace et al. 1998; Hsu and Liu et al. 2003; Stevenson et al. 2015). The ongoing global warming under anthropogenic greenhouse gases (GHG) forcing has substantial impacts on not only the mean-state climate but also climate variability. Knowing whether the interannual climate variability amplifies or not under global warming is crucial for mitigation and adaptation strategies for climate change.

It is widely accepted that El Niño-Southern Oscillation (ENSO) is the strongest signal of interannual climate variability in the tropics, and great efforts have been devoted

Electronic supplementary material The online version of this article (<https://doi.org/10.1007/s00382-018-4286-0>) contains supplementary material, which is available to authorized users.

✉ Tim Li
timli@hawaii.edu

¹ Institute for Environmental and Climate Research, Jinan University, Guangzhou, China

² Key Laboratory of Meteorological Disaster of Ministry of Education, Nanjing University of Information Science and Technology, Nanjing, China

³ International Pacific Research Center and Department of Atmospheric Sciences, University of Hawaii, Honolulu, USA

to the future change of ENSO and its impact (e.g., Collins et al. 2010; Cai et al. 2014). It is agreed that ENSO will still be the dominant mode of interannual climate variability in future (Stevenson et al. 2012), and the impact of ENSO on global climate will be strengthened although the amplitude of the SST variability of ENSO stays generally unchanged (Cai et al. 2014; Watanabe et al. 2014; Bonfils et al. 2015). Besides tropical Pacific, the interannual precipitation variability over North America would be amplified by enhanced atmospheric teleconnection pattern associated with ENSO (Simon Wang et al. 2015; Yoon et al. 2015). The interannual variability of atmospheric circulation over western North Pacific driven by ENSO or ENSO-related Sea Surface Temperature (SST) anomalies may also be amplified (Hu et al. 2014; Tao et al. 2015; Chen et al. 2016).

However, interannual climate variability can be stimulated by lots of factors while ENSO is only one of them. Outside the tropics, ENSO only explains a small fraction of the total interannual climate variability (Dai and Wigley 2000; Ferguson et al. 2010). Agriculture production and human society are affected by not only ENSO but the total interannual climate variability (Mearns et al. 1992; Kummur et al. 2014), therefore it will be as important to examine the possible change of the total amplitude of interannual climate variability besides ENSO-related interannual variability. Both observational and modeling studies reported an intensification of interannual rainfall variability over certain regions, including equatorial Pacific and the Asian monsoon region (Lu and Fu 2010; Fu 2012; Seager et al. 2012; Menon et al. 2013; Fan et al. 2014; Chen et al. 2017), but the response of atmospheric circulation to SST anomaly seems to be weakened (Huang et al. 2017).

Precipitation is regulated by thermodynamic and dynamic components. Constrained by Clausius–Clapeyron relation, atmospheric water vapor content increases by about 6–7% per degree of warming (Held and Soden 2006; Schneider et al. 2010), and a wind convergence anomaly could generate a stronger water vapor convergence anomaly in a moister atmosphere even if the wind convergence anomaly itself is unchanged (Seager et al. 2012; Pendergrass and Gerber 2016), acting to enhance the interannual rainfall variability. The dynamic factor for rainfall variability originates from the changes in the variability of wind, therefore it can be theoretically hypothesized that enhanced/weakened interannual circulation variability could enhance/weaken the interannual precipitation variability (Lu and Fu 2010; Huang and Xie 2015). Meanwhile, the amplitude of interannual rainfall variability is constrained by the abundance of mean state rainfall (Watanabe et al. 2014; He et al. 2017a), and more abundant mean state rainfall is usually associated with greater interannual rainfall variability.

Atmospheric circulation variability has a major contribution to precipitation variability. Tropical atmospheric circulation anomalies are modulated by both diabatic heating anomalies and static stability (Schneider et al. 2010; Ma et al. 2012; Li et al. 2015), since the horizontal temperature gradient and transient eddy flux are weak. And this relationship is also valid in the summertime subtropics (Liu et al. 2004; Li et al. 2012). If the rainfall variability is enhanced/reduced, as demonstrated by previous studies, the variability of atmospheric diabatic heating associated with latent heating will also be enhanced/reduced, and the enhanced/reduced diabatic heating variability acts to enhance/reduce the circulation variability (Cai et al. 2014; Li et al. 2015). On the other hand, previous studies claimed an enhanced static stability of the troposphere under global warming (Knutson and Manabe 1995; Schneider et al. 2010). The increase of static stability acts to weaken the mean state circulation (Ma et al. 2012; Qu and Huang 2016; Sohn et al. 2016; He et al. 2017b), but its impact on the amplitude of interannual circulation variability still needs to be assessed.

Up to now, there is still a lack of a quantitative assessment on the response of the amplitude of interannual variability of precipitation and circulation to GHG forcing, and the relative contributions from their controlling factors. By using the outputs from the models participating in Coupled Model Intercomparison Project Phase 5 (CMIP5; Taylor et al. 2012), we aim at clarifying the following scientific questions in this study: How does the amplitude of interannual variability of precipitation and circulation respond to GHG forcing? Which factors are responsible for the pattern and magnitude of the response? Simple theoretical explanations are proposed and tested in this study, to understand the projected changes in the interannual variability of rainfall and circulation.

The rest of the paper is organized as follows. The model and methods are introduced in Sect. 2, and a brief evaluation of the model simulations against the observational datasets is performed in Sect. 3. The projected changes of the interannual variability by CMIP5 models are elaborated in Sect. 4, and the possible mechanisms for the response in the interannual variability are investigated in Sect. 5 and Sect. 6 for precipitation and circulation, respectively. The conclusion and discussion are finally presented in Sect. 7.

2 Model, data and methods

Totally 30 models from CMIP5 are adopted in this study, to evaluate the possible response of the amplitude of interannual climate variability to GHG forcing. The models used in this study are listed in Table S1 in the Supplementary Information, and monthly outputs of the Historical, Representative Concentration Pathway 8.5 (RCP8.5) and

RCP4.5 experiments are adopted for analyses. The Historical experiment is performed by forcing the coupled models with observed historical external forcing (GHG, aerosol, etc) from 1850 to 2005, while RCP8.5/RCP4.5 experiments are performed by forcing coupled models with a rising GHG concentration toward a future radiative forcing of $8.5 \text{ Wm}^{-2}/4.5 \text{ Wm}^{-2}$ at the year of 2100 (Vuuren et al. 2011). The RCP8.5 scenario represents a business-as-usual high emission pathway toward an equivalent CO₂ concentration of about 1370 ppm by the year of 2100, while the RCP4.5 represents an intermediate mitigation pathway in which the CO₂ concentration stabilizes at about 650 ppm after 2100.

Given the observational uncertainty (Collins et al. 2013), multiple observational and reanalysis datasets are adopted to evaluate the simulation of the climate in Historical experiment. The precipitation datasets include global precipitation climatology project (GPCP) version 2 (Adler et al. 2003) and CPC Merged Analysis of Precipitation (CMAP; Xie and Arkin 1997). The reanalysis datasets on atmospheric circulation include National Centers for Environmental Prediction-Department of Energy reanalysis version 2 (NCEP2; Kanamitsu et al. 2002) and ERA-Interim reanalysis (ERA-Interim; Dee et al. 2011). Due to the available observational data length, the period of 1980–1999 in the Historical experiment is evaluated against the observation.

Difference between the late twenty-first century (2050–2099, 21C for short) of RCP8.5 experiment with the late twentieth century (1950–1999, 20C for short) of Historical experiment is calculated for each model, and the multi-model median (MMM) of the differences is calculated to suppress the model bias and internal variability. Multi-model median is superior to multi-model mean in representing the forced response since it is robust to outliers (Gleckler et al. 2008). The inter-model consistency (or uncertainty) among the MMM-projected change by the 30 models is evaluated, in terms of the percentage of the individual models which agree in sign with the MMM-projected change. According to Power et al. (2012), a 95% significance level based on *t*-test is equivalent to an inter-model consistency of 68% under the assumption of independency among the models, and a slightly stricter threshold of 70% is adopted here to test the inter-model consistency. The results based on the difference between RCP4.5 and Historical experiments are also examined and discussed, to evaluate the robustness of the results.

We mainly focus on precipitation and vertical velocity over 20°S–50°N in June–July–August (JJA) in this study, and the projected changes per degree of surface warming are investigated. Vertical velocity is adopted to measure the circulation variability since it is essential to precipitation (e.g., Chou et al. 2009; Chen and Bordoni 2016). For the time series of precipitation (P) and vertical velocity (ω), the interannual variability components (P' and ω') are obtained by an 8-year high-pass Fourier filter, and their standard

deviations ($\sigma(P')$, $\sigma(\omega')$) are obtained, to evaluate the amplitude of interannual variability. The projected absolute change of a variable X per degree of warming (for example, $X = \sigma(P')$) is denoted as ΔX , which is the difference between 21C and 20C scaled by the mean surface warming, i.e., $\Delta X = (X^{21C} - X^{20C}) / (T^{21C} - T^{20C})$, and $T^{21C} - T^{20C}$ is the mean amplitude of surface warming within 20°S–50°N. And the fractional change in X per degree of warming is denoted as δX , which is the ratio between the absolute change and its mean state in 20C, i.e., $\delta X = \Delta X / X^{20C}$ (the unit is %K⁻¹). The projected changes by the individual models are calculated before obtaining the multi-model median (MMM).

3 The simulated and observed amplitude of interannual variability

The MMM-simulated interannual standard deviation of precipitation and vertical velocity at 500 hPa in Historical experiment are shown in Fig. 1, in comparison with multiple observational datasets. It is clear that the spatial pattern of the interannual standard deviation of precipitation ($\sigma(P')$) generally follows the spatial pattern of mean state precipitation (\bar{P} , the contours), in both the models and the two observational datasets (Fig. 1a–c). The spatial pattern of $\sigma(P')$ in MMM resembles those in the observational datasets, with a pattern correlation of 0.85 with either GPCP or CMAP. There is large discrepancy among the GPCP and CMAP datasets, especially around the tropical western Pacific where the $\sigma(P')$ and the mean state precipitation in CMAP dataset are much higher than in GPCP dataset. Such observational uncertainty has also been noted by previous studies (Yin et al. 2004; Collins et al. 2013).

Variability of vertical velocity at the mid-troposphere is claimed to be essential for the variability of precipitation (e.g., Seager et al. 2012; Huang and Xie 2015; Wen et al. 2015; Chen and Bordoni 2016; Long et al. 2016). The $\sigma(\omega')$ at 500 hPa is generally greater over the climatological ascending regions than in the climatological descending regions, in both the MMM and the observational datasets (Fig. 1d–f). A comparison between the mean state precipitation and mean state vertical velocity suggests that the zero contour of mean state vertical velocity at 500 hPa generally overlaps the 200 mm contour of mean state precipitation in JJA, in both the MMM and the observational datasets (contours in Fig. 1) The climatological ascending regions are generally associated with abundant mean state rainfall and larger $\sigma(P')$, which may stimulate a larger interannual variability of atmospheric circulation through diabatic heating (He et al. 2017a). The $\sigma(\omega')$ at 500 hPa is much higher over the equatorial regions in NCEP2 dataset than in ERA-Interim dataset (Fig. 1e, f), suggesting a great

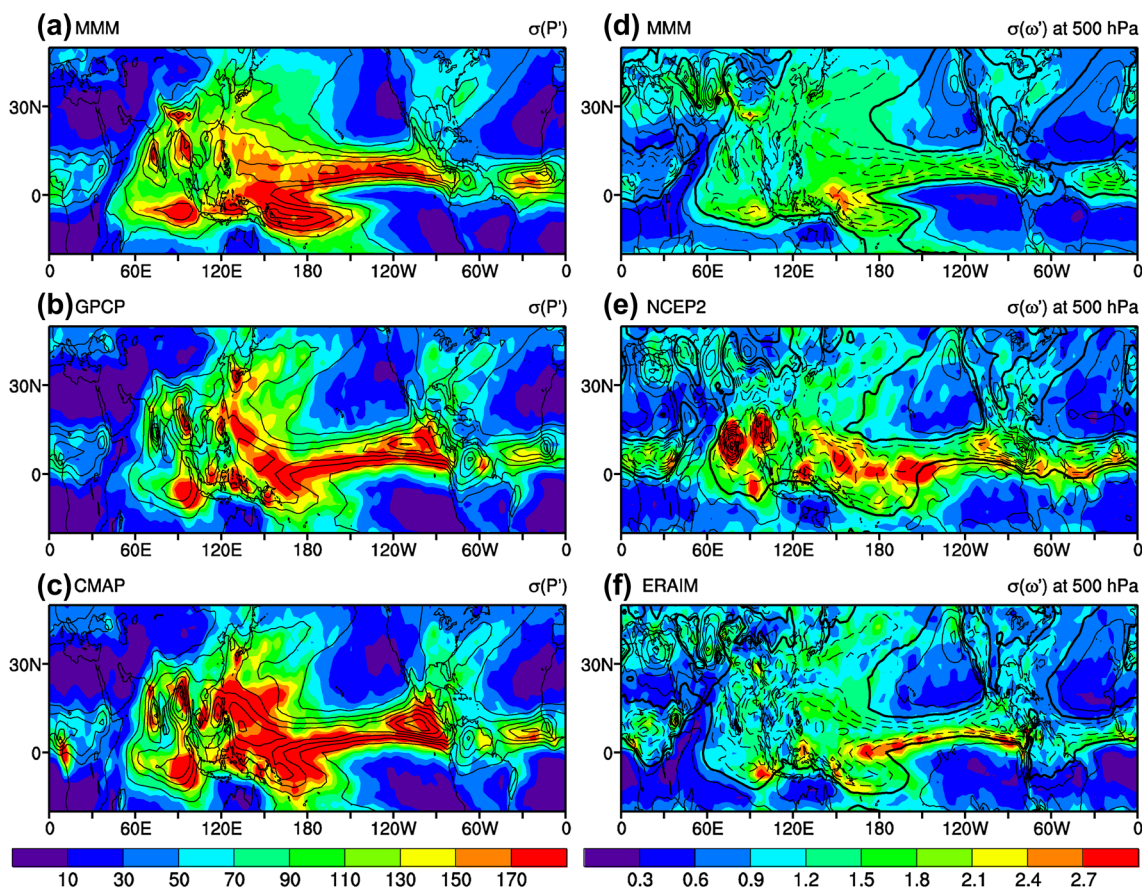


Fig. 1 The mean state (contours) and interannual standard deviation (shading) for precipitation ($\sigma(P')$, unit: mm) and vertical velocity at 500 hPa ($\sigma(\omega')$, unit: $10^{-2} \text{ Pa s}^{-1}$) in JJA. The contours for \bar{P} starts at 200 mm with an interval of 200 mm in **a–c**, and the contour interval for $\bar{\omega}$ is $2 \times 10^{-2} \text{ Pa s}^{-1}$ with dashed negative contours and bold zero

contours in **d–f**. **a, d** Are based on the MMM of Historical simulation, the precipitation in **b** and **c** are based on the GPCP and CMAP datasets, respectively, and the vertical velocity in **e** and **f** are based on NCEP2 and ERAIM datasets, respectively

observational uncertainty. The MMM-simulated $\sigma(\omega')$ at 500 hPa is more consistent with ERAIM dataset than with NCEP2 dataset.

Given the large observational uncertainty among observational datasets, it is currently hard to select a subset of high-skill models which have smaller difference with the observation or using the observational constraint approach (Brown et al. 2017; Li et al. 2017). On the other hand, the MMM captures the overall spatial pattern and magnitude of both $\sigma(P')$ and $\sigma(\omega')$, suggesting the formation mechanism for the overall spatial pattern and the amplitude of interannual variability is captured by the MMM, and it is reasonable to use the MMM of the 30 models to assess the response of the amplitude of interannual variability to GHG forcing. The use of a large ensemble of models will help to suppress the internal variability and random bias of the individual models, which is superior to a subset of few models (Deser et al. 2010).

4 Projected changes in the amplitude of interannual variability

The MMM-projected percentage change of interannual standard deviation under GHG forcing is shown in Fig. 2, for precipitation (P') and vertical velocity (ω') at 500 hPa. Consistent with Watanabe et al. (2014), the $\sigma(P')$ increases substantially for more than 30% K^{-1} over some parts of equatorial Pacific, and the regional average over $5^{\circ}\text{S}–5^{\circ}\text{N}$, $180^{\circ}–90^{\circ}\text{W}$ is $16.5\% \text{ K}^{-1}$. The $\sigma(P')$ also increases over a large area from South Asia to Northwest Pacific Ocean, but decreases over a major part of the subtropical areas. The regional averaged amplitude of $\delta\sigma(P')$ within $20^{\circ}\text{S}–50^{\circ}\text{N}$ is $1.4\% \text{ K}^{-1}$. The sign of $\delta\sigma(P')$ seems to be related to the climatological vertical velocity. Most of the climatological ascending regions are dominated by increased $\sigma(P')$, while a substantial part of the climatological descending

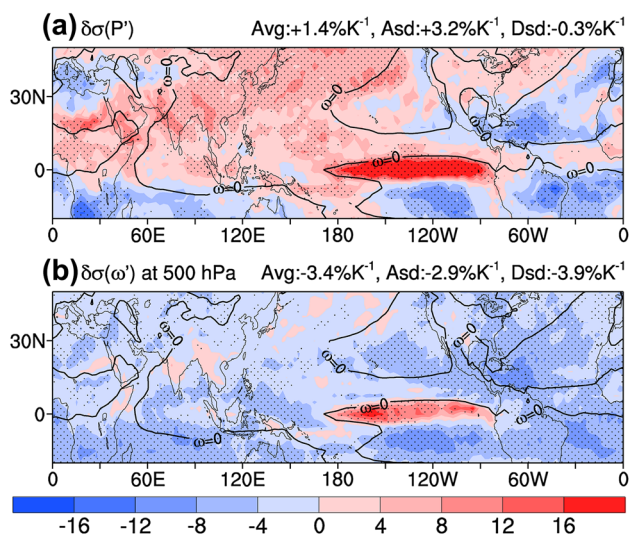


Fig. 2 Percentage change of the standard deviation at interannual timescale for precipitation (a) and vertical velocity (b) scaled by surface warming (unit: $\%K^{-1}$) based on RCP8.5 and Historical experiments. Thick black line indicates the zero contour of mean state vertical velocity at 500 hPa in the Historical simulation. All the phenomena are based on the multi-model median (MMM), whereas the projected changes agreed by more than 70% of the individual models are stippled. The regional averaged changes for the whole region, the climatological ascending region (Asd) and the climatological descending region (Dsd) are marked on the upper-right corner of each panel

regions are dominated by decreased $\sigma(P')$ except equatorial Pacific. The regional averaged $\delta\sigma(P')$ within the climatological ascending regions and descending regions are $3.2\% K^{-1}$ and $-0.3\% K^{-1}$, respectively. Excluding the equatorial Pacific ($5^{\circ}S-5^{\circ}N$, $180^{\circ}-90^{\circ}W$), the regional averaged $\delta\sigma(P')$ over the other parts of the descending regions is $-1.7\% K^{-1}$. In general, $\delta\sigma(P')$ tends to increase over climatological ascending regions and the equatorial Pacific, but decrease over the subtropical subsidence regions.

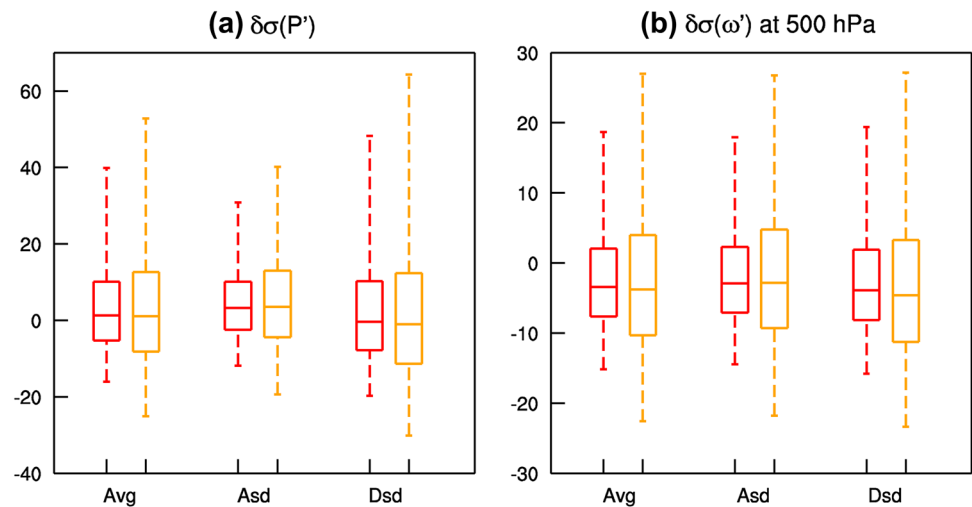
Previous studies also suggested enhanced interannual variability of precipitation over most areas of the globe except the subtropical subsidence regions (Seager et al. 2012; Pendergrass et al. 2017), but the detailed number of change differs among the studies due to different regions, seasons are focused on and different metrics are adopted. Based on multiple models from CMIP3, Seager et al. (2012) reported a decrease of the interannual variability of annual mean precipitation minus evaporation ($P - E$) over a substantial area in the subtropical subsidence regions but an increase elsewhere. Based on RCP8.5 experiment of CMIP5 models, Pendergrass et al. (2017) reported a decrease in both interannual and intraseasonal precipitation variability over subtropical subsidence regions and an increase elsewhere, and they claimed an global averaged increase of precipitation

variability of $3-4\% K^{-1}$. Our results about the change in $\sigma(P')$ is consistent with previous studies in terms of its spatial pattern and overall magnitude. Most of the previous studies adopted multi-model mean, but one important caution is that multi-model mean value over arid area may be severely distorted by outlier models, since the climatological $\sigma(P')$ over the arid area is very small in some models and an increase of $\sigma(P')$ could give rise to a very high $\delta\sigma(P')$. Indeed, there are 103 grid points in the individual models with a $\delta\sigma(P')$ of higher than $400\%K^{-1}$, and all of these outlier grid points are located at the arid area in climatological descending region. These outliers severely bias the multi-model mean (Fig. S1 in Supplementary Information), but has little impact on the multi-model median, confirming the superiority of the median to mean (Glecker et al. 2008).

In contrast to the generally enhanced precipitation variability, $\sigma(\omega')$ at 500 hPa is projected to decrease over most tropical and subtropical regions, but increases over a narrow band at equatorial Pacific (Fig. 2b), which is consistent with Seager et al. (2012). The regional averaged $\delta\sigma(\omega')$ within $20^{\circ}S-50^{\circ}N$ is $-3.4\% K^{-1}$. Unlike the opposite signs of $\delta\sigma(P')$ between the averages in climatological ascending and descending regions, the averaged $\delta\sigma(\omega')$ over ascending and descending regions are $-2.9\% K^{-1}$ and $-3.9\% K^{-1}$, respectively. Even in the equatorial Pacific, the magnitude of the increase in $\sigma(\omega')$ does not exceed $20\% K^{-1}$, and the regional average over $5^{\circ}S-5^{\circ}N$, $180^{\circ}-90^{\circ}W$ is $6.2\% K^{-1}$, much smaller than the local increase in $\sigma(P')$. Excluding equatorial Pacific, the regional averaged $\delta\sigma(\omega')$ over other parts of the descending regions is $-4.7\%K^{-1}$. There is seemingly a mechanism which acts to suppresses $\sigma(\omega')$ globally.

In order to examine the inter-model uncertainty and the dependence of the results on the emission scenario, Fig. 3 compares the regional averaged values between RCP8.5 and RCP4.5 scenarios in terms of box-whisker plot. The MMM of the regional averaged fractional changes per degree of warming under RCP4.5 are very close to those under RCP8.5, regardless of the entire domain, the ascending region or the descending region (Fig. 3). The spatial pattern of the projected changes under RCP4.5 (Fig. S2 in the Supplementary Information) also closely resembles those under RCP8.5. Meanwhile, the range of the inter-model uncertainty, as indicated by the range between the 25th and 75th percentiles or the range between the maximum and the minimum, is smaller under RCP8.5 scenario than RCP4.5 scenario (Fig. 3), possibly because of the stronger forced response relative to the internal variability under the high emission pathway of RCP8.5. The difference of the MMM between RCP4.5 and RCP8.5 is negligible compared with the large inter-model uncertainty, suggesting the percentage change per degree of warming does not depend obviously on the emission scenario. Previous study focused on extreme precipitation and heat waves also revealed similar rate of change per degree of warming under RCP8.5

Fig. 3 Box-whisker plot for the regional averaged percentage changes (unit: %K⁻¹) in the interannual variability of precipitation (a) and vertical velocity at 500 hPa (b), showing the minimum, the 25th percentile, the median, the 75th percentile and the maximum among the 30 models. The projected regional averaged changes for the entire domain over 20°S–50°N (Avg), the ascending regions (Asd) and the descending regions (Dsd) are shown, and the red and the orange boxes are based on RCP8.5 and RCP4.5 experiments, respectively



and RCP4.5 scenarios (Donat et al. 2016; Perkins-Kirkpatrick and Gibson 2017), suggesting the scenario-uncertainty can be suppressed if we focus on the *changes per degree of warming*. To be brief, the analyses in the rest of the paper are based on RCP8.5.

The above evidences suggest that the interannual variability of precipitation generally intensifies but the interannual variability of vertical velocity generally weakens under GHG forcing, but their spatial patterns are complicated. Although the standard deviation (or variance) of geopotential height increase under global warming condition (Lu and Fu 2010; Lee et al. 2014), it may not indicate an increase in the interannual variability of atmospheric circulation, since the circulation is determined by the horizontal gradient rather than the absolute magnitude of geopotential height (He et al. 2015; Huang et al. 2016; Chen and Bordoni 2016). The enhanced variability of geopotential height is actually a result of the increased variability of tropospheric temperature, according to the hypsometric equation (Hu et al. 2014, 2017; He et al. 2015). The mechanism for the pattern and magnitude of the responses will be addressed in the next two sections for precipitation and circulation, respectively.

5 Mechanism for the change in interannual rainfall variability

In order to understand the mechanism for the projected change of $\sigma(P')$ in terms of its magnitude and spatial pattern, we try to construct a theoretical framework by simplifying the moisture budget equation. Following Chou et al. (2009), the moisture budget equation is written as

$$P = E - \left\langle \omega \frac{\partial q}{\partial p} \right\rangle - \langle \mathbf{V} \cdot \nabla q \rangle + R \tag{1}$$

where P , E , q , ω , and \mathbf{V} represent precipitation, evaporation, specific humidity, vertical velocity and horizontal wind vector, respectively. R is the residual, and $\langle \cdot \rangle = g^{-1} \int_{ps}^{pt} \cdot dp$ denotes column integration from surface to the top of the atmosphere. The column integrated vertical moisture advection term $-\langle \omega \frac{\partial q}{\partial p} \rangle$ is equivalent to column integrated horizontal wind convergence expressed as $-\langle q \nabla \cdot \mathbf{V} \rangle$ in some previous studies (Seager et al. 2010; Lin et al. 2014). Designating the mean state of each variable with an overbar and the anomaly at interannual timescale with a prime, the anomaly of precipitation at interannual timescale can be approximated by

$$P' \approx E' - \left\langle \omega' \frac{\partial \bar{q}}{\partial p} \right\rangle - \left\langle \bar{\omega} \frac{\partial q'}{\partial p} \right\rangle - \langle V' \cdot \nabla \bar{q} \rangle - \langle \bar{V} \cdot \nabla q' \rangle \tag{2}$$

In Eq. (2), the higher-order terms and the residual are omitted. Based on an evaluation on the relative importance of the five terms on the right-hand side of Eq. (2) (Fig. S6 in the Supplementary Information), $-\langle \omega' \frac{\partial \bar{q}}{\partial p} \rangle$ dominates the phase and amplitude of the interannual variability of P' , since it has a greater temporal correlation and a smaller root-mean-square deviation with P' than the other four terms. Previous studies also claimed that the anomalous vertical advection of mean state moisture (equivalent to the anomalous convergence/divergence of mean state moisture) is the most important contributor to precipitation variability (Seager et al. 2012; Li et al. 2013; Lin et al. 2014; Huang and Xie 2015; Wang et al. 2017a; Wu et al. 2017). Over the arid land regions, P' has the highest correlation with E' (Fig. S6a in the Supplementary Information), but the interannual variability of E' is constrained by P' rather than constraining P' . As $-\langle \omega' \frac{\partial \bar{q}}{\partial p} \rangle$ is the most important contributor to P' , Eq. (2) can be approximated as

$$P' \approx - \left\langle \omega' \frac{\partial \bar{q}}{\partial p} \right\rangle \quad (3)$$

Equation (3) involves vertical gradient of specific humidity and vertical integration. It can be further simplified by a two-layer conceptual model, where the averaged specific humidity at the upper and lower layers is used to approximate the vertical gradient of specific humidity. Therefore, Eq. (3) can be further approximated as

$$P' \approx -\omega'_m (\bar{q}_l - \bar{q}_u) / g \quad (4)$$

where g is gravitational acceleration, ω'_m stands for the vertical velocity at the mid-troposphere, and q_l and q_u are the specific humidity for the lower and upper troposphere. Many previous studies used the vertical velocity at 500 hPa to approximate the dynamic contribution to precipitation (e.g., Wen et al. 2015; Chen and Bordoni 2016; Long et al. 2016). Following these studies, ω'_m is approximated by the vertical velocity at 500 hPa. Since specific humidity of the atmosphere damps exponentially upward from the surface, \bar{q}_l and \bar{q}_u are approximated by the specific humidity at 925 and 400 hPa, respectively. An examination shows that it is reasonable to approximate $-\left\langle \omega' \frac{\partial \bar{q}}{\partial p} \right\rangle$ with $-\omega'_m (\bar{q}_l - \bar{q}_u) / g$, since the high temporal correlation and low root-mean-square deviation between P' and $-\left\langle \omega' \frac{\partial \bar{q}}{\partial p} \right\rangle$ is not destroyed by such approximation (Fig. S7a,d in Supplementary Information).

As mean state specific humidity at lower troposphere is much higher than at upper troposphere, $\bar{q}_l - \bar{q}_u \approx \bar{q}_l$, and Eq. (4) can be further simplified as

$$P' \approx -\omega'_m \bar{q}_l / g \quad (5)$$

Omitting the upper-level specific humidity has almost no impact on the accuracy of the conceptual model (Fig. S7b,e in Supplementary Information). According to Eq. (5), P' is approximately proportional to ω'_m at interannual timescale., since the \bar{q}_l is constant under a given climate background. Therefore, $\sigma(P') \approx -\sigma(\omega'_m) \bar{q}_l / g$ should be hold for both 20C and 21C. As $\sigma(P')$ is approximately proportional to the product of $\sigma(\omega'_m)$ and \bar{q}_l , the fractional change of $\sigma(P')$ can be approximated by the sum of the fractional changes in $\sigma(\omega'_m)$ and \bar{q}_l (see the “Appendix A” for detailed derivation), i.e.,

$$\delta\sigma(P') \approx \delta\sigma(\omega'_m) + \delta\bar{q}_l \quad (6)$$

Figure 4a shows the fractional change of mean state specific humidity at 925 hPa ($\delta\bar{q}_l$), and Fig. 4b shows $\delta\sigma(\omega'_m) + \delta\bar{q}_l$ ($\delta\sigma(\omega'_m)$ is already shown in Fig. 2b), in order to examine whether the theoretical prediction by Eq. (6) agrees with the projected $\delta\sigma(P')$. The projected $\delta\bar{q}_l$ is positive everywhere and the regional average is $6.4\% \text{ K}^{-1}$, consistent with the prediction by Clausius–Clapeyron relationship (Held and Soden 2006; Schneider et al. 2010). The increase of \bar{q}_l is slightly stronger along the equator and at the mid latitudes,

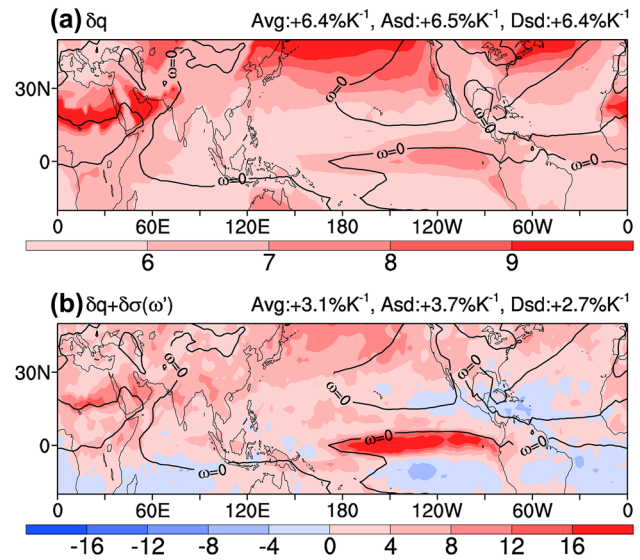


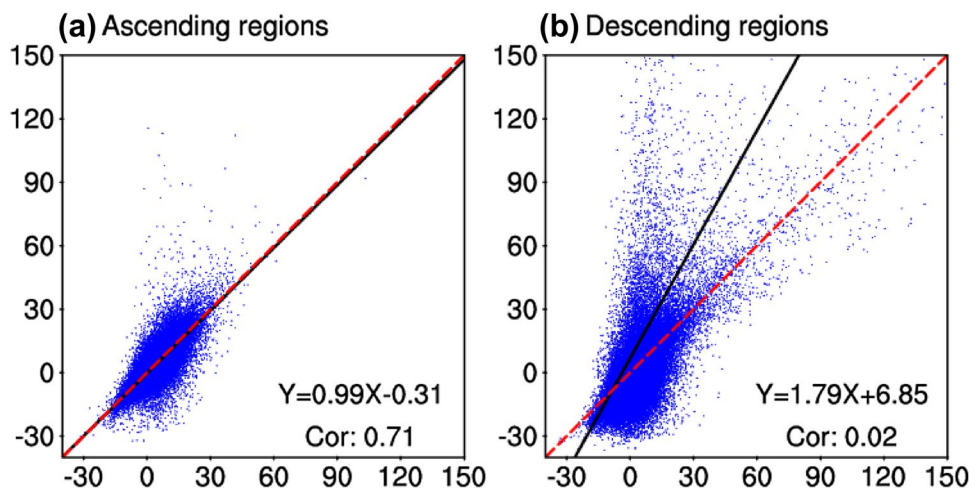
Fig. 4 **a** The MMM-projected percentage change in the mean state specific humidity at 925 hPa ($\delta\bar{q}_l$) per degree of warming (unit: $\% \text{K}^{-1}$). **b** The sum of MMM-projected percentage changes in the mean state specific humidity and the standard deviation of vertical velocity at interannual time scale, i.e., $\delta\sigma(\omega'_m) + \delta\bar{q}_l$. The black contour indicates the MMM-simulated zero contour of climatological vertical velocity at 500 hPa

but relatively weak on the southern and northern flanks of the equator (Fig. 4a), consistent with the SST warming pattern (Zhang and Li 2014). According to Eq. (6), the increase low-level specific humidity contributes to a relatively uniform increase of $\delta\sigma(P')$ for about $6.4\% \text{ K}^{-1}$.

The sum of $\delta\sigma(\omega'_m)$ and $\delta\bar{q}_l$ reproduces the general pattern of projected $\delta\sigma(P')$ (Fig. 4b), and its pattern correlation coefficient with Fig. 2a is 0.81. Compared with the projected $\delta\sigma(P')$ by CMIP5 models in Fig. 2a, the approximation by Eq. (6) reproduces the strong increase of $\sigma(P')$ over equatorial Pacific, modest increase of $\sigma(P')$ over ascending regions, and decrease of rainfall variability over the subtropics. However, the approximation in Eq. (6) underestimates the decrease of $\sigma(P')$ over subtropical descending regions. The regional averaged $\delta\sigma(\omega'_m) + \delta\bar{q}_l$ over ascending regions (based on the mean state vertical velocity of MMM) is $+3.7\% \text{ K}^{-1}$, close to the projection by CMIP5 models. But the regional averaged $\delta\sigma(\omega'_m) + \delta\bar{q}_l$ over the descending region is $+2.7\% \text{ K}^{-1}$, far from the projected $\delta\sigma(P')$, primarily due to the overestimation in the subtropical subsidence region. In all, the theoretical prediction by Eq. (6) captures the fractional change in the interannual rainfall variability over climatological ascending regions but does not perform well in the subsidence regions.

To further examine the relationships between $\delta\sigma(P')$ and $\delta\sigma(\omega'_m) + \delta\bar{q}_l$ in terms of spatial pattern and inter-model spread, Fig. 5 shows the scatter diagram between $\delta\sigma(P')$ and $\delta\sigma(\omega'_m) + \delta\bar{q}_l$ among all grid points of all models.

Fig. 5 Scatter diagram about the percentage changes in the interannual precipitation variability ($\delta\sigma(P')$, y-axis) as a function of $\delta\sigma(\omega'_m) + \delta\bar{q}_l$ (x-axis), for all the grid points within climatological ascending (a) and descending (b) regions of all individual models. The black line is the least-square regression line and the red dashed line is the diagonal line of $Y=X$. The least-square regression equation and the correlation coefficient for each panel are marked on the lower-right corner



Given the mean state differs among models, each grid point of an individual model within 20°S – 50°N is categorized into either climatological ascending regions or descending regions, based on the climatological vertical velocity at 500 hPa in the Historical experiment of the model itself (not based on the MMM). Over ascending regions, $\delta\sigma(P')$ is linearly related with $\delta\sigma(\omega'_m) + \delta\bar{q}_l$. The least-square fit line almost overlaps the diagonal line of $Y = X$, and the correlation coefficient is 0.71 (Fig. 5a), suggesting the theoretical model of Eq. (6) well explains the spatial pattern and inter-model spread in climatological ascending regions. Over the descending regions, the correlation coefficient between $\delta\sigma(P')$ and $\delta\sigma(\omega'_m) + \delta\bar{q}_l$ is 0.02 and the regression line deviates from the diagonal line (Fig. 5b). There are some outliers with a very high $\delta\sigma(P')$ at some grid point over the arid descending regions of some models, since the $\sigma(P')$ is too small in Historical experiment and a modest increase of $\sigma(P')$ could induce a very high $\delta\sigma(P')$. Even if the outliers with a $\delta\sigma(P')$ of higher than $400\% \text{ K}^{-1}$ (totally 103 grid points) are excluded, the $\delta\sigma(P')$ over descending regions is not so closely related to $\delta\sigma(\omega'_m) + \delta\bar{q}_l$ as in the ascending regions, and the regression slope is 1.20 (Fig. S8). It again suggests that Eq. (6) does not give an as good estimation of $\delta\sigma(P')$ in descending regions as in ascending regions.

The theoretical model in Eq. (6) does not work well in descending regions possibly due to the scarce mean state precipitation, and as a result the rainfall anomaly is insensitive to anomalous vertical moisture advection. For example, in the years with negative precipitation anomaly, there is almost no precipitation here, and a stronger negative vertical moisture advection anomaly due to increased specific humidity could not further enhance the negative precipitation anomaly. Since the magnitude of rainfall variability is also constrained by the abundance of mean state rainfall (Watanabe et al. 2014; He et al. 2017a), the relationship between the mean state precipitation (\bar{P}) and the magnitude of interannual precipitation

variability ($\delta\sigma(P')$) based on all the grid points of all individual models is examined in Fig. 6a, b. Over the descending regions, $\delta\sigma(P')$ is closely correlated with \bar{P} , and the regression equations are $\sigma(P') = 0.30\bar{P} + 6.08$ and $\sigma(P') = 0.34\bar{P} + 3.50$ for Historical and RCP8.5 experiments, respectively. The intercept of the regression line is small and negligible, and $\sigma(P')$ is nearly proportional to \bar{P} , i.e., $\sigma(P') \propto \bar{P}$. Under the assumption of proportionality between $\sigma(P')$ and \bar{P} over descending regions, the fractional change in the interannual rainfall variability should be equal to the fractional change in the mean state rainfall, i.e.,

$$\delta\sigma(P') \approx \delta\bar{P} \quad (7)$$

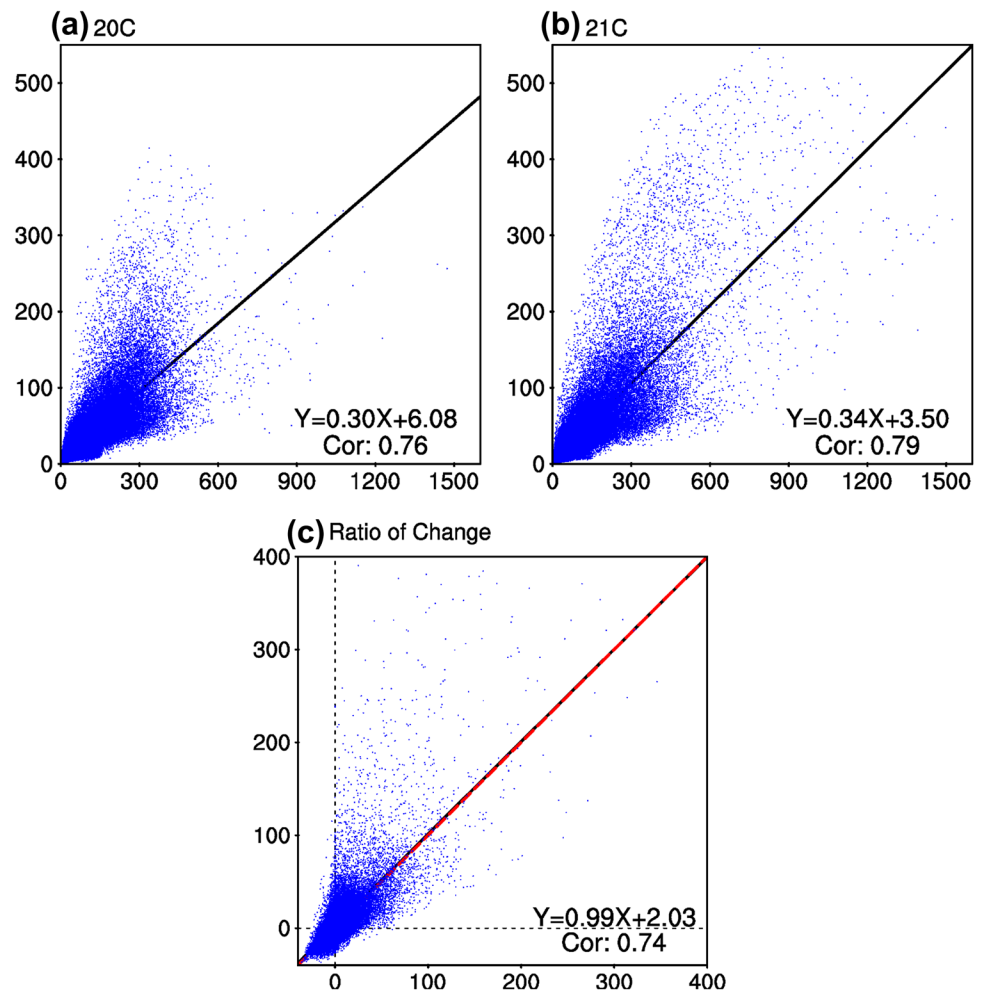
Thus the theoretical model in Eq. (5) can be adjusted as

$$\delta\sigma(P') \approx \begin{cases} \delta\sigma(\omega'_m) + \delta\bar{q}_l & \text{if } \bar{\omega}_m < 0 \\ \delta\bar{P} & \text{if } \bar{\omega}_m > 0 \end{cases} \quad (8)$$

The relationship between $\delta\sigma(P')$ and $\delta\bar{P}$ for the grid points of all models in the descending regions is shown in Fig. 6c (the 103 grid points in the 30 models with a $\delta\sigma(P')$ greater than $400\% \text{ K}^{-1}$ are excluded). It is clear that the regression line almost overlaps the diagonal line of $Y=X$, with a regression slope of 0.99, suggesting relationship of $\delta\sigma(P') \approx \delta\bar{P}$ is valid over the descending regions.

The spatial pattern of $\delta\bar{P}$ projected by the MMM is shown in Fig. 7a. The mean state precipitation increases sharply over equatorial Pacific, possibly due the local maximum amplitude of SST warming (Watanabe et al. 2014; Li et al. 2016). It also increases substantially over the monsoon region from Asia to West Pacific, consistent with the “richest-get-richer” mechanism (Zhang and Li 2017). The reduced \bar{P} over the descending regions at the subtropics may be modulated by the dry horizontal advection (Chou et al. 2009) or changes in mean state circulation associated with land-sea thermal contrast (He and Soden 2017).

Fig. 6 Scatter diagram for the grid points located at descending regions of all individual models. **a** The interannual precipitation variability ($\sigma(P')$, y-axis) as a function of mean state precipitation (\bar{P} , x-axis) for 20C in Historical experiment (unit: mm). **b** Same as **(a)** but for 21C in RCP8.5 experiment. **c** Percentage change in the interannual precipitation variability ($\delta\sigma(P')$, y-axis) as a function of the percentage change in mean state precipitation ($\delta\bar{P}$, x-axis). The black line is the least-square regression line, and the dashed red line in **(c)** is the diagonal line of $Y=X$



The pattern of $\delta\bar{P}$ looks like $\delta\sigma(P')$, but the regional averaged $\delta\bar{P}$ within 20°S – 50°N is $0.4\% \text{K}^{-1}$, much lower than $\delta\sigma(P')$. This regional averaged percentage is lower than the global averaged value of $2\% \text{K}^{-1}$ obtained by Held and Soden (2006) but with no contradiction. Held and Soden (2006) addressed the fractional change of global averaged rainfall, and their fractional change was computed after averaging global rainfall, so the wet regions (i.e., ascending regions) contribute more than the dry regions (i.e., descending regions) to the average. But our study shows the average of the fractional changes, and the fractional change at each grid point is computed before taking regional average, so that dry regions and wet regions are equally weighted.

Figure 7b shows the estimation of $\delta\sigma(P')$ based on Eq. (7). Given the mean state differs among models, the estimation based on Eq. (7) is made for each model according to the mean state vertical velocity (ω_m) of the individual model itself, and MMM of the estimated $\delta\sigma(P')$ by the 30 models is shown. The regional average

within 20°S – 50°N is $+1.4\% \text{K}^{-1}$ (Fig. 7b), well matching the projected $\delta\sigma(P')$ (Fig. 2a). The averaged values over the ascending and descending regions of the MMM is $+3.4\% \text{K}^{-1}$ and $-0.4\% \text{K}^{-1}$, respectively (Fig. 7b), also well matching the projected $\delta\sigma(P')$. Under RCP4.5 scenario, the theoretical framework in Eq. (8) also explains the projected $\delta\sigma(P')$ almost exactly (Fig. S3 in Supplementary Information). The salient features in Fig. 2a, such as the substantially increased rainfall variability over equatorial Pacific, the modest increase in the climatological ascending regions, and the decrease over subtropical oceans, are well reproduced by Eq. (8) (Fig. 7b). The pattern correlation between Figs. 7b and 2a is 0.87. Therefore, the theoretical model in Eq. (8) gives a satisfactory estimation of the magnitude and spatial pattern of the projected changes in interannual precipitation variability, for both ascending and descending regions.

Can Eq. (8) explain the inter-model uncertainty on the projected $\delta\sigma(P')$ and which term in Eq. (8) contributes the most to the inter-model uncertainty? Figure 8a shows the spatial pattern for the inter-model correlation coefficients

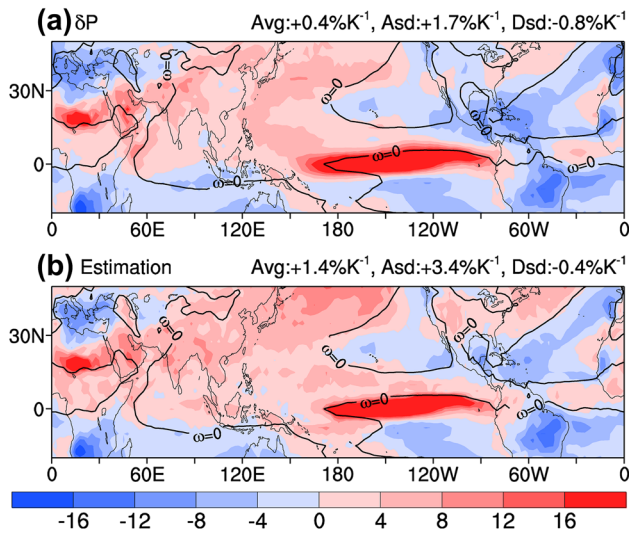


Fig. 7 **a** The MMM-projected percentage change in the mean state precipitation per degree of warming (unit: $\%K^{-1}$). **b** The estimation of $\delta\sigma(P')$ based on Eq. (8), i.e., the multi-model median of $\delta\sigma(\omega'_m) + \delta\bar{q}_l$ in ascending regions and $\delta\bar{P}$ over descending regions of the individual models. The black contour is the zero contour of mean state vertical velocity at 500 hPa

between projected $\delta\sigma(P')$ and the estimation based on Eq. (8). It is obvious that the inter-model correlation is significant at the 95% confidence level for almost all grid points (Fig. 8a), suggesting the theoretical model in Eq. (8) accounts for the inter-model uncertainty. As suggested by the inter-model correlation between projected $\delta\sigma(P')$ and each term in Eq. (8) (Fig. 8b–d), the inter-model correlation between $\delta\sigma(P')$ and $\delta\bar{q}_l$ is much weaker than the inter-model correlation between $\delta\sigma(P')$ and $\delta\sigma(\omega'_m)$ over climatological ascending regions (Fig. 8b, c), and the $\delta\sigma(P')$ over descending regions has a much higher inter-model correlation with $\delta\bar{P}$ than with $\delta\bar{q}_l$ or $\delta\sigma(\omega'_m)$. Previous study also indicated that the increase of specific humidity contributes to a uniform increase of extreme precipitation, whereas the regional pattern and inter-model uncertainty is dominated by circulation changes (Pfahl et al. 2017). Our evidences suggest that the inter-model uncertainty of the changes in $\sigma(P')$ is dominated by the uncertainty of circulation variability over ascending region but by mean state rainfall in descending region.

Based on the above analyses, the mechanism for the projected change of interannual precipitation variability is different between ascending regions and descending regions. Over climatological ascending regions, $\sigma(P')$ is modulated by vertical moisture advection which is contributed by the abundance of mean state specific humidity and the interannual variability of vertical velocity. The percentage change in $\sigma(P')$ is well explained by the sum of the percentage changes

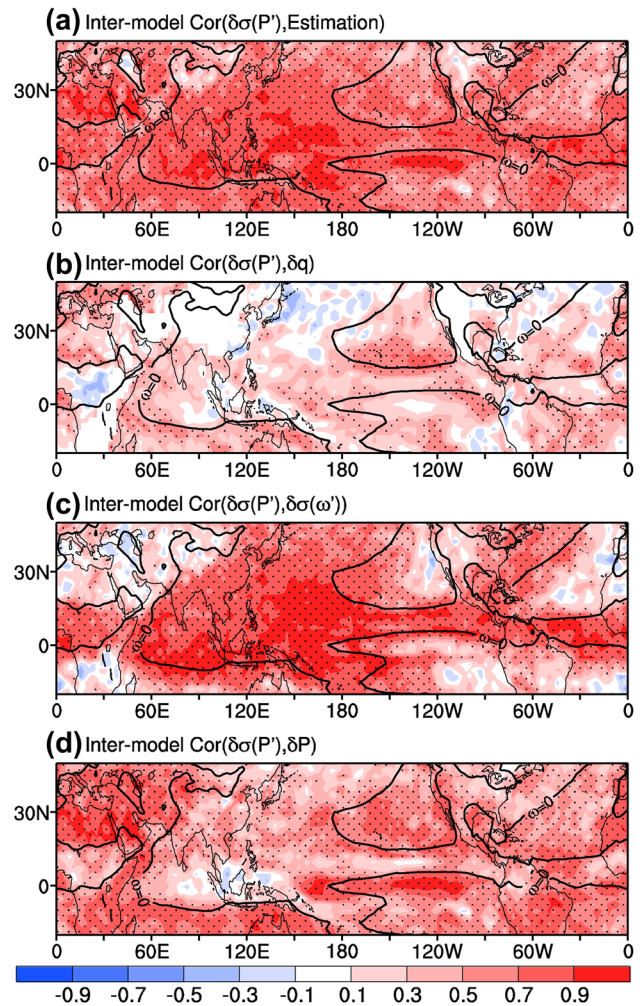


Fig. 8 **a** Inter-model correlation coefficients between projected $\delta\sigma(P')$ and the estimated change based on Eq. (8). **b–d** Inter-model correlation coefficients of the projected $\delta\sigma(P')$ with $\delta\bar{q}_l$ (**b**), $\delta\sigma(\omega'_m)$ (**c**) and $\delta\bar{P}$ (**d**). The correlation coefficients significant at the 95% confidence level according to *t*-test are stippled. The black contour is the zero contour of mean state vertical velocity at 500 hPa

in low-level specific humidity (\bar{q}_l) and the magnitude of variability of mid-tropospheric vertical velocity ($\sigma(\omega'_m)$). However, $\sigma(P')$ is strongly constrained by the abundance of mean state precipitation over climatological descending regions (i.e., dry regions), where the percentage change of $\sigma(P')$ almost equals to the percentage change in mean state precipitation. The inter-model uncertainty for the projected change in $\sigma(P')$ is dominated by the interannual variability of vertical velocity in ascending regions but by the mean state precipitation over descending regions. Further effort is needed to narrow the uncertainty of the projected change in $\sigma(P')$.

6 Mechanism for the change in interannual circulation variability

The atmospheric circulation in the tropics and summer-time subtropics is driven by diabatic heating (Rodwell and Hoskins 2001; Liu et al. 2004; Li et al. 2012), and the interannual variability of diabatic heating explains a substantial fraction of the interannual circulation variability (Wei et al. 2014; Leonardo and Hameed 2015; Zhang et al. 2016). Indeed, the interannual standard deviation of column diabatic heating is projected to get enhanced (weakened) where the interannual precipitation variability is enhanced (weakened), and its change is dominated by latent heating associated with precipitation variability (Fig. S9 in Supplementary Information). Such enhanced variability of diabatic heating acts to enhance the interannual variability of atmospheric circulation (Cai et al. 2014; Chung and Power 2016). On the other hand, the static stability of the troposphere also increases under global warming, as a result of moist adiabatic adjustment (Knutson and Manabe 1995; Schneider et al. 2010). In a more stable atmosphere, a weaker circulation anomaly could be stimulated by a diabatic heating anomaly (Ma et al. 2012; Li et al. 2015). Following previous studies (Li et al. 2015; Pendergrass and Gerber 2016), horizontal temperature gradient can be omitted and the thermodynamic equation is simplified as

$$Q \approx -S\omega \tag{9}$$

where Q , S , ω are diabatic heating, static stability and vertical velocity. Therefore, the anomaly of diabatic heating at interannual timescale is balanced by

$$Q' \approx -\bar{S}\omega' - S'\bar{\omega} \tag{10}$$

where bar and prime stand for the mean state and anomaly, respectively, and the higher-order term ($S'\bar{\omega}$) is omitted. At interannual time scale, the contribution of $S'\bar{\omega}$ to Q' is much smaller than $\bar{S}\omega'$ and can be neglected (Fig. S10 in the Supplementary Information). So, the anomaly of vertical velocity can be expressed as

$$\omega' \approx -Q'/\bar{S} \tag{11}$$

According to Eq. (11), the interannual standard deviation of circulation is expressed as $\sigma(\omega') \approx -\sigma(Q')/\bar{S}$ since the mean state static stability \bar{S} has no temporal variation for a given climate background, and the fraction of change in $\sigma(\omega')$ can be estimated by the fractional changes of $\sigma(Q')$ and \bar{S} (See Appendix A for detailed derivation), i.e.,

$$\delta\sigma(\omega') \approx \delta\sigma(Q') - \delta\bar{S} \tag{12}$$

To examine whether Eq. (12) explains the projected change in $\sigma(\omega')$, the diabatic heating is calculated based on the thermodynamic equation following Yanai and Tomita (1998), and the fractional changes of $\sigma(Q')$, \bar{S} , and their difference at 500 hPa are shown in Fig. 9. The

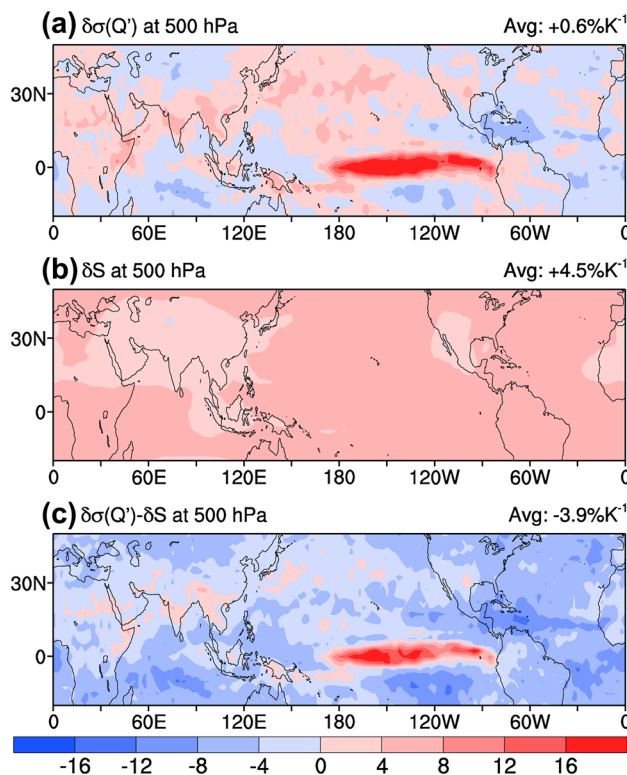


Fig. 9 Projected percentage changes of a the interannual variability of diabatic heating ($\delta\sigma(Q')$), b mean state static stability ($\delta\bar{S}$), and c their difference ($\delta\sigma(Q') - \delta\bar{S}$) at the isobaric surface of 500 hPa per degree of warming (unit: $\% K^{-1}$)

interannual variability of diabatic heating enhances substantially at equatorial Pacific for as much as $20\% K^{-1}$, and it also enhances modestly from South Asia to western North Pacific but slightly weakens over the most subtropical oceans, consistent with the projected change in rainfall variability (Fig. 2a). The static stability at 500 hPa increases everywhere and it has a rather spatially uniform pattern (Fig. 9b), contributing to a rather uniform decrease of $\sigma(\omega')$ according to Eq. (12). The difference of $\delta\sigma(Q')$ and $\delta\bar{S}$ (Fig. 9c) well reconstructs the pattern of $\delta\sigma(\omega')$ at 500 hPa, including the obvious increase along the equatorial Pacific and a modest decrease elsewhere. The pattern correlation between $\delta\sigma(Q') - \delta\bar{S}$ and $\delta\sigma(\omega')$ at 500 hPa is 0.77. The regional averaged $\delta\sigma(Q')$ and $\delta\bar{S}$ over $20^{\circ}S-50^{\circ}N$ are $0.6\% K^{-1}$ and $4.5\% K^{-1}$, contributing to a regional averaged $\delta\sigma(Q') - \delta\bar{S}$ of $-3.9\% K^{-1}$, suggesting a slight overestimation of the decrease in $\sigma(\omega')$. This overestimated decrease in $\sigma(\omega')$ is mainly contributed by the extratropical region within $40^{\circ}N-50^{\circ}N$. Over $20^{\circ}S-40^{\circ}N$, the regional averaged $\delta\sigma(\omega')$ is $-3.6\% K^{-1}$ and $\delta\sigma(Q') - \delta\bar{S}$ is $-3.8\% K^{-1}$, which are very close to each other. In all, Eq. (12) gives a satisfactory estimation of the projected fractional change in the interannual circulation variability at 500 hPa, especially over the tropics.

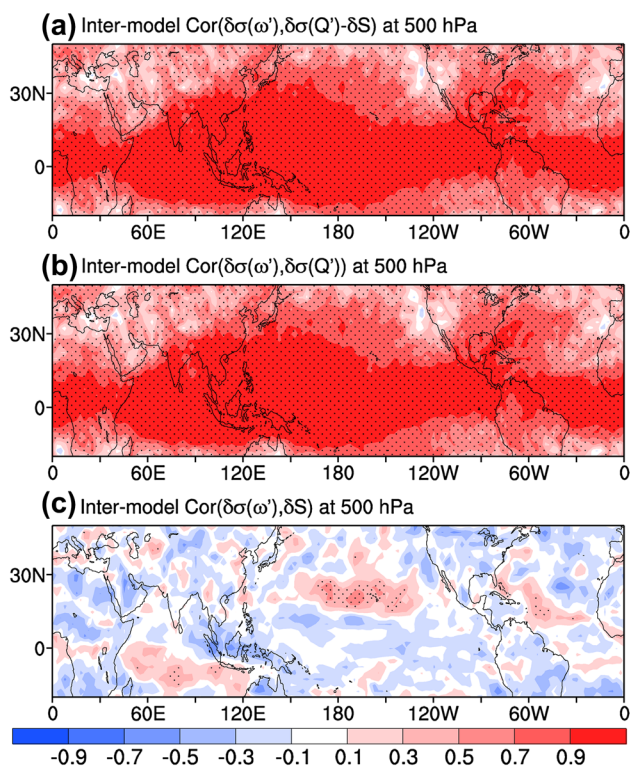


Fig. 10 **a** Inter-model correlation coefficients between $\delta\sigma(\omega')$ and $\delta\sigma(Q') - \delta\bar{S}$ at 500 hPa. **b–c** Inter-model correlation coefficients between $\delta\sigma(\omega')$ with $\delta\sigma(Q')$ (**b**) and $\delta\bar{S}$ (**c**). The correlation coefficients significant at the 95% confidence level according to *t*-test are stippled

The inter-model uncertainty of the projected change in $\delta\sigma(\omega')$ is also highly correlated with the inter-model uncertainty in $\delta\sigma(Q') - \delta\bar{S}$ (Fig. 10a), suggesting the theoretical model in Eq. (12) well captures the inter-model uncertainty of the projected change in $\sigma(\omega')$. The inter-model correlation between $\delta\sigma(\omega')$ and $\delta\sigma(Q')$ exceeds the 95% confidence level according to *t*-test at almost all grid points (Fig. 10b), resembling the correlation pattern between $\sigma(\omega')$ and $\delta\sigma(Q') - \delta\bar{S}$. But the inter-model correlation between $\delta\sigma(\omega')$ and $\delta\bar{S}$ is weak and insignificant at almost all grid points (Fig. 10c). These evidences suggest that the inter-model uncertainty in the projected change in $\sigma(\omega')$ is dominated by the inter-model uncertainty in the changes in $\sigma(Q')$, whereas the inter-model uncertainty in the mean state static stability makes a negligible contribution.

To address whether the vertical structure of projected $\delta\sigma(\omega')$ can be explained by Eq. (12), Fig. 11 shows the vertical profiles of $\delta\sigma(Q')$, $\delta\bar{S}$ and their difference, in comparison with the projected $\delta\sigma(\omega')$. $\delta\sigma(Q')$ intensifies at the mid-to-upper troposphere along the equator and over subtropical South Asia to West Pacific (Fig. 11a, b), consistent with enhanced convective rainfall variability in these regions because the enhanced latent heating associated with deep

convection is located at mid-to-upper troposphere (Li et al. 2015). The intensification is especially strong over the equatorial Pacific, acting to enhance the local interannual variability of atmospheric circulation (Cai et al. 2014, 2015). On the other hand, the static stability increases at almost all pressure levels below 200 hPa (Fig. 11c, d), acting to reduce the circulation variability everywhere, according to Eq. (12). The increase of static stability reaches its maximum at about 300–400 hPa, consistent with Li et al. (2015).

The longitude-height profile of $\delta\sigma(Q') - \delta\bar{S}$ well resembles the projected $\delta\sigma(\omega')$ over both equatorial region and the subtropical region (Fig. 11e, f). At the equatorial region (averaged within 5°S–5°N), $\delta\sigma(Q') - \delta\bar{S}$ is positive over the Pacific sector but negative elsewhere, with an average of $-0.6\% \text{ K}^{-1}$, close to the averaged value of 0.0% of the projected $\delta\sigma(\omega')$, with a pattern correlation coefficient of 0.95 between $\delta\sigma(Q') - \delta\bar{S}$ and $\delta\sigma(\omega')$ (Fig. 11e). At the subtropical northern hemisphere (averaged within 20°–30°N), $\delta\sigma(Q') - \delta\bar{S}$ and $\delta\sigma(\omega')$ are negative at almost all longitudes through the troposphere, and they are more negative over the subtropical Atlantic but approaches zero over subtropical Asia–West Pacific. The averaged values are $-1.7\% \text{ K}^{-1}$ for $\delta\sigma(Q') - \delta\bar{S}$ and $-1.3\% \text{ K}^{-1}$ for $\delta\sigma(\omega')$, with a pattern correlation of 0.87. In all, the combined effect of increased mean state static stability and the change in diabatic heating variability well explains the overall vertical structure of $\delta\sigma(\omega')$.

In order to examine whether the spatial pattern of the projected $\delta\sigma(\omega')$ is captured by the theoretical model in Eq. (12) at each pressure level, $\delta\sigma(\omega')$ at all the grid points of all the individual models are plotted in Fig. 12 as a function of $\delta\sigma(Q') - \delta\bar{S}$. The correlation coefficient between $\delta\sigma(\omega')$ and $\delta\sigma(Q') - \delta\bar{S}$ ranges from 0.73 to 0.91 from 850 to 200 hPa, but is relatively low at 925 hPa (0.47). The regression slopes for the pressure levels within 850 and 200 hPa ranges from 0.63 to 0.82, which are slightly smaller than 1, indicating that the spatial variation of $\delta\sigma(\omega')$ is overestimated by the theoretical model in Eq. (12). The regression relationship between $\delta\sigma(\omega')$ and $\delta\sigma(Q') - \delta\bar{S}$ for MMM is similar to those based on all the individual models (Fig. S11 in Supplementary Information). Although the estimation based on Eq. (12) does not exactly reproduce the spatial variation of $\delta\sigma(\omega')$, especially at 925 hPa, the results have shown that it well reproduces the overall horizontal and vertical pattern and regional averaged magnitude of $\delta\sigma(\omega')$, under both RCP8.5 and RCP4.5 scenarios (see Figs. S4, S5 for the results under RCP4.5 scenarios).

Based on the above theoretical formulation and diagnostic analyses, the response of the magnitude of interannual circulation variability to GHG forcing is generally controlled by two factors: mean state static stability and the variability of diabatic heating. The static stability shows a horizontally uniform increase throughout the troposphere as a result of moist adiabatic adjustment (Knutson and Manabe 1995;

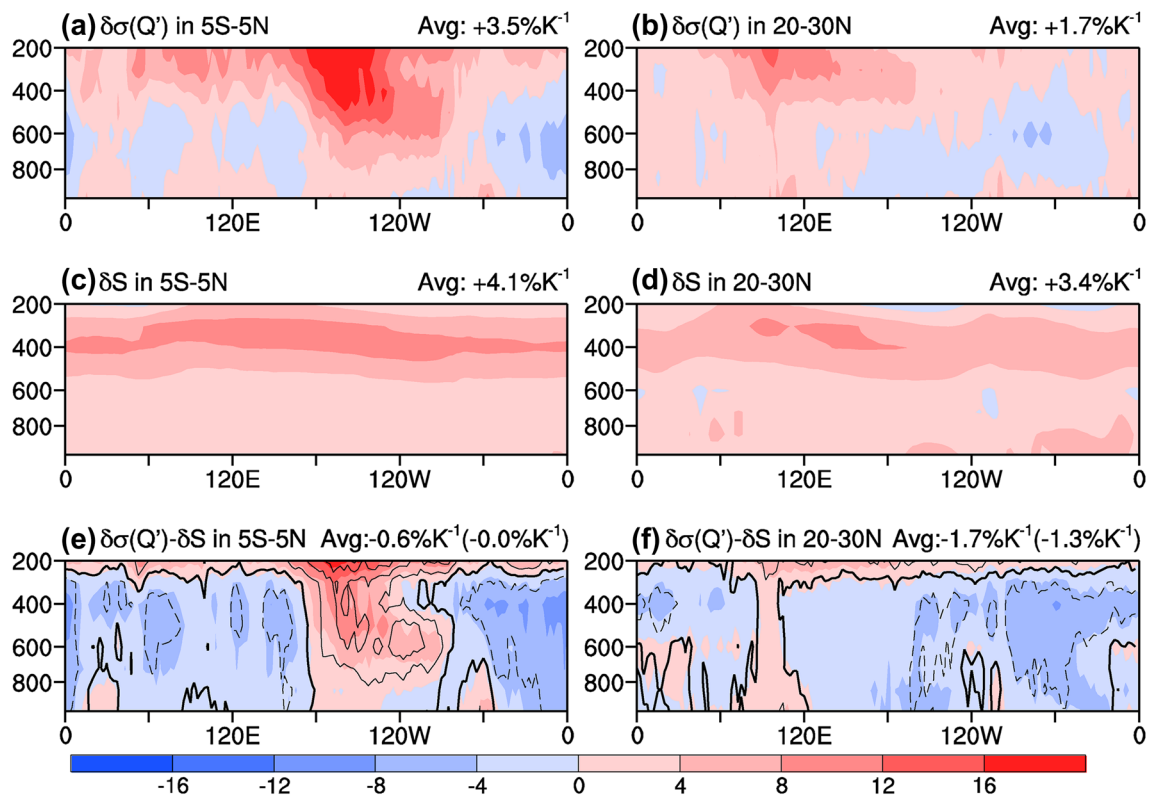


Fig. 11 Same as Fig. 9, but for the longitude-height profiles of the averaged values within 5°S–5°N (left column) and within 20°–30°N (right column). The contours in (e) and (f) show the MMM-projected $\delta\sigma(\omega')$, and the contour interval is exactly the same as the shading.

The average value for the shading in each panel is marked on its upper-right corner, and the averaged value for the MMM-projected $\delta\sigma(\omega')$ is marked in the parenthesis in (e, f)

Schneider et al. 2010), and it acts to reduce the amplitude of interannual variability of vertical velocity. The change in the variability of diabatic heating, which dominates the intermodel uncertainty of projected $\delta\sigma(\omega')$, is mainly contributed by latent heating associated with precipitation. It enhances where $\sigma(P')$ enhances at the mid-upper troposphere, especially over equatorial Pacific. Therefore, the changes in $\sigma(P')$ and $\sigma(\omega')$ may be coupled with each other: On the one hand, increased (decreased) circulation variability acts to enhance (reduce) the rainfall variability. On the other hand, increased (decreased) rainfall variability enhances (reduces) local diabatic heating variability and further enhances (reduces) circulation variability.

7 Conclusion and discussion

In this study, the response of the amplitude of interannual climate variability to GHG forcing is assessed, by comparing the RCP8.5/RCP4.5 experiment with Historical experiment based on CMIP5 models. The amplitude of interannual variability is measured by the standard deviation (σ) of 8-year high-pass filtered time series, and the magnitude

and spatial pattern of the changes in the interannual variability of precipitation and circulation (vertical velocity) are assessed. By constructing and validating theoretical models, the relative contributions of the factors responsible for the changes in precipitation and circulation are addressed. In general, the projected changes are similar between RCP8.5 and RCP4.5, in terms of the spatial pattern and the regional averaged changes per degree of warming. The responses of the interannual variability of precipitation and circulation under global warming are modulated by the changes in the mean states of precipitation, specific humidity and static stability, which are summarized in Fig. 13 and as follows.

(1) The interannual variability of precipitation generally amplifies but its spatial pattern is complicated. The interannual variability of rainfall amplifies substantially over equatorial Pacific, and it also increases modestly in the climatological ascending regions, but decreases over the subtropical areas where the mean state rainfall decreases, with a regional averaged $\delta\sigma(P')$ of $1.4\% K^{-1}$. The interannual precipitation variability is constrained by mean state precipitation in the descending regions but by vertical moisture advection in ascending regions. Over the descending regions with relatively scarce mean state rainfall, the

Fig. 12 Scatter diagram for the projected changes in $\delta\sigma(\omega')$ (y-axis, unit: $\% \text{ K}^{-1}$) as a function of $\delta\sigma(Q') - \delta\bar{S}$ (x-axis, unit: $\% \text{ K}^{-1}$) for all the grid points of all the individual models at each pressure level. The solid black line is the least-square regression line, and the dashed red line is the $Y=X$ line

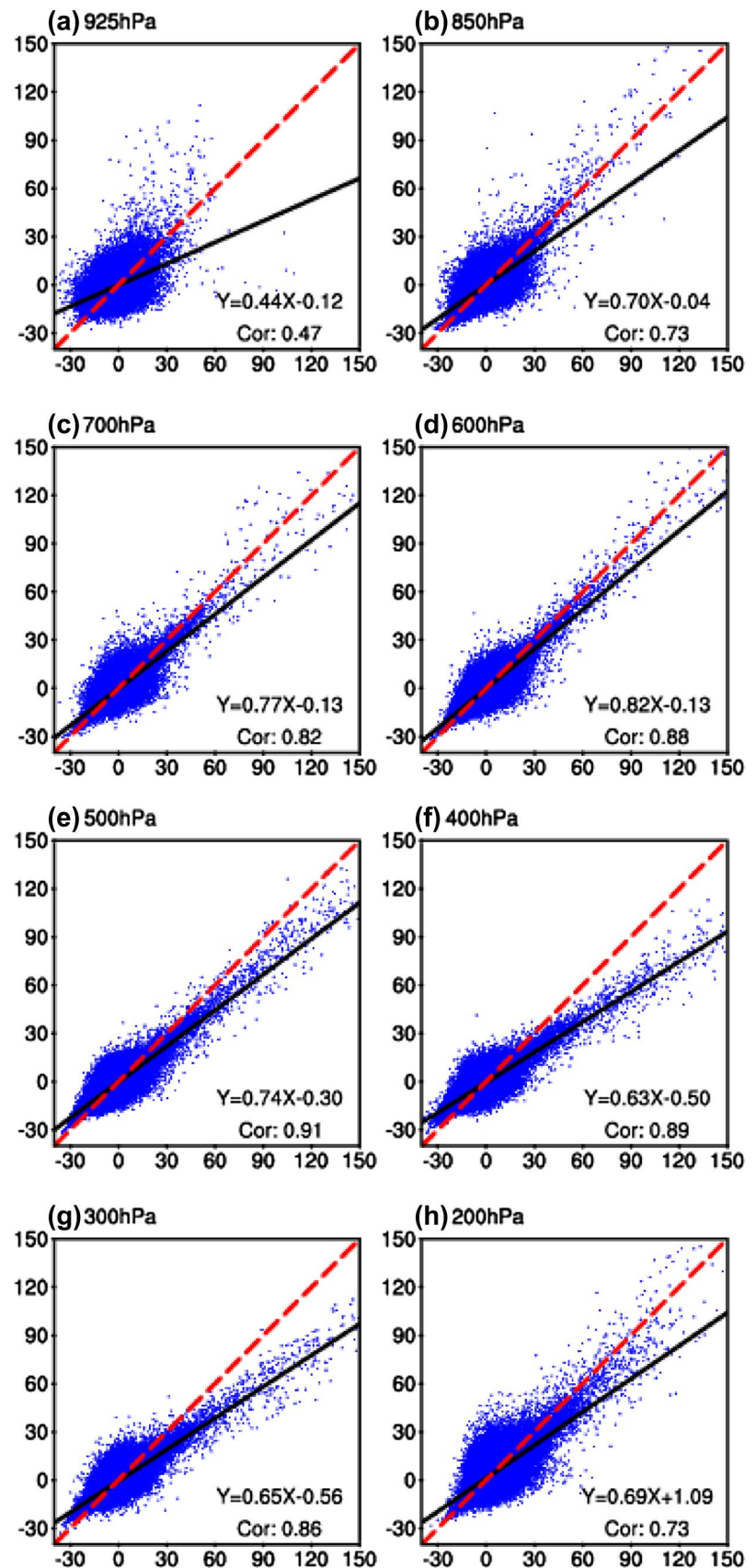
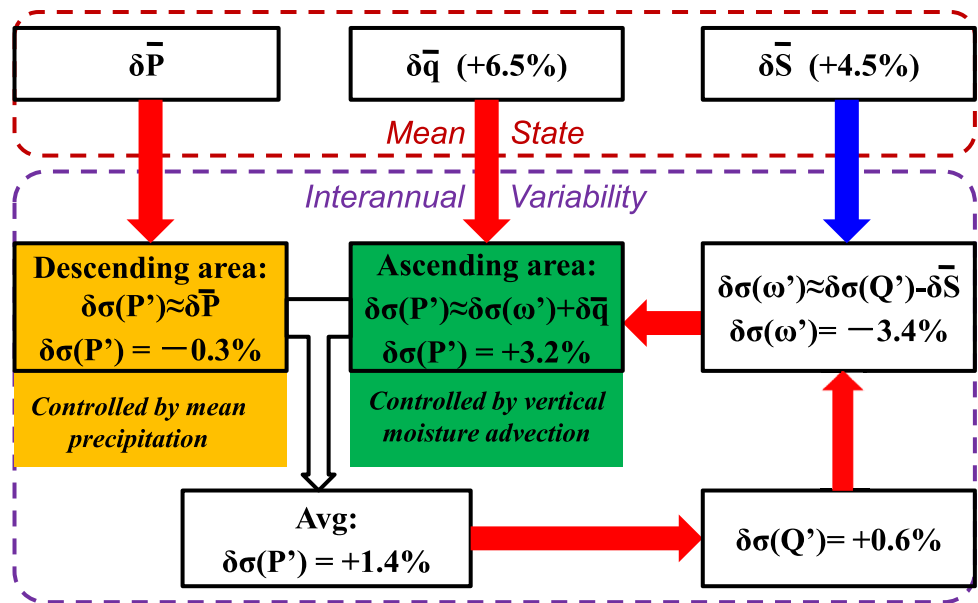


Fig. 13 A schematic illustrating the mechanisms for the changes in the interannual variability of precipitation and circulation. The red arrows indicate that positive (negative) change in the former box acts to induce positive (negative) change in the next box, whereas blue arrow indicates that positive (negative) change in the former box acts to induce negative(positive) change in the next box. As static stability, vertical velocity and diabatic heating are 3-dimensional phenomenon, their regional averaged values are 500 hPa are listed



magnitude of interannual precipitation variability is almost proportional to the abundance of mean state precipitation, and the percentage change of interannual precipitation variability approximately equals to the percentage change of the mean state precipitation, i.e., $\delta\sigma(P') \approx \delta\bar{P}$. Over climatological ascending regions with abundant mean state precipitation, the advection of mean state humidity by anomalous vertical velocity is essential for the interannual variability of precipitation, and $\delta\sigma(P')$ is determined by the changes in the specific humidity at lower troposphere and the interannual variability of vertical velocity at mid troposphere, i.e., $\delta\sigma(P') \approx \delta\sigma(\omega'_m) + \delta\bar{q}_l$. In addition, the inter-model uncertainty of projected $\delta\sigma(P')$ is dominated by $\delta\sigma(\omega'_m)$ over ascending regions but by $\delta\bar{P}$ over descending regions.

(2) The interannual variability of vertical velocity enhances over equatorial Pacific at mid-upper troposphere but weakens elsewhere, with a regional averaged amplitude of $-3.4\% \text{ K}^{-1}$ at 500 hPa. The response of interannual circulation variability is modulated by mean state static stability and the interannual variability of diabatic heating, through the relation $\delta\sigma(\omega') \approx \delta\sigma(Q') - \delta\bar{S}$. The static stability increases almost everywhere in the troposphere with a maximum magnitude at the upper troposphere, and it acts to weaken the interannual variability of vertical velocity through the troposphere. The interannual variability of diabatic heating enhances substantially over equatorial Pacific at the mid-to-upper troposphere, which overwhelms the effect of increased static stability and enhances the local circulation variability. The change in the interannual variability of diabatic heating is mainly contributed by the changed variability of latent heating associated with precipitation variability, and it dominates the inter-model uncertainty of the projected changes in the interannual variability of vertical velocity.

The pattern and magnitude of the change in the interannual variability for precipitation and vertical velocity are addressed in this study, since these two variables are closely coupled with each other (Seager et al. 2012; Pendergrass and Gerber 2016). Enhanced interannual variability of precipitation may be associated with an enhancement of the hydrological extremes, such as enhanced extreme precipitation (Trenberth et al. 2003; Liu et al. 2016; Pendergrass et al. 2017), and the increased intensity of typhoons despite of large uncertainty (Knutson et al. 2010; Park et al. 2017). In addition, the interannual variability of temperature also greatly impacts human society, and previous studies claimed a generally enhanced variability of tropospheric temperature over the entire tropics (Hu et al. 2014; Tao et al. 2015). The increase of the mean state temperature and the enhanced temperature variability may both have contributions to the temperature extremes, especially heat waves (Fischer et al. 2012; Sun et al. 2014; Holmes 2016; Wang et al. 2017b), but their relative contributions to cold waves and heat waves still reserve further assessment.

Acknowledgements This work was supported by National Key Research and Development Program of China (2017YFA0604601), the National Natural Science Foundation of China (41505067), the United States National Science Foundation (AGS-1565653) and Open Research Fund Program of Key Laboratory of Meteorological Disaster of Ministry of Education (KLME1601). The authors wish to acknowledge the modeling groups and PCMDI for providing modeling data.

Appendix A

Suppose a variable X is proportional to the product of the variables Y and Z , i.e., $X = kYZ$ where k is a non-zero constant. In a warmer climate, all of these three variable will change. If we denote the mean state in 20C with an overbar and the absolute change in 21C relative to 20C with a prefix of Δ , the relationship between these three variables for 21C is expressed as

$$\bar{X} + \Delta X = k(\bar{Y} + \Delta Y)(\bar{Z} + \Delta Z) = k\bar{Y}\bar{Z} + k\bar{Y}\Delta Z + k\bar{Z}\Delta Y + k\Delta Y\Delta Z \quad (13)$$

Since $\bar{X} = k\bar{Y}\bar{Z}$ holds for the 20C, and the high-order term $\Delta Y\Delta Z$ is generally small and negligible, Eq. (13) can be simplified into

$$\Delta X = k\bar{Y}\Delta Z + k\bar{Z}\Delta Y \quad (14)$$

Since $\bar{X} = k\bar{Y}\bar{Z}$, if the left-hand side of Eq. (14) is divided by \bar{X} and the right-hand side of Eq. (14) is divided by $k\bar{Y}\bar{Z}$, the following relation is obtained

$$\Delta X/\bar{X} = \Delta Y/\bar{Y} + \Delta Z/\bar{Z} \quad (15)$$

If the prefix “ δ ” to adopted to denote the relative change of a variable to its climatology in 20C, Eq. (15) can be expressed as

$$\delta X = \delta Y + \delta Z \quad (16)$$

In all, if variable X is proportional to the product of the variables Y and Z , the percentage change in X under global warming is the sum of the percentage changes in Y and Z . Similarly, if the variable Z is proportional to the quotient between X and Y , i.e., $Z = kX/Y$, the relationship $\delta Z = \delta X - \delta Y$ can also be obtained.

References

- Adler RF, Huffman GJ, Chang A, Ferraro R, Xie PP, Janowiak J, Rudolf B, Schneider U, Curtis S, Bolvin D, Gruber A, Susskind J, Arkin P, Nelkin E (2003) The version-2 global precipitation climatology project (GPCP) monthly precipitation analysis (1979-present). *J Hydrometeorol* 4(6):1147–1167. [https://doi.org/10.1175/1525-7541\(2003\)004%3C1147:tvGPCP%3E2.0.CO;2](https://doi.org/10.1175/1525-7541(2003)004%3C1147:tvGPCP%3E2.0.CO;2)
- Bonfils CJW, Santer BD, Phillips TJ, Marvel K, Leung LR, Doutriaux C, Capotondi A (2015) Relative contributions of mean-state shifts and ENSO-driven variability to precipitation changes in a warming climate. *J Clim* 28(24):9997–10013. <https://doi.org/10.1175/jcli-d-15-0341.1>
- Brown PT, Caldeira K (2017) Greater future global warming inferred from Earth’s recent energy budget. *Nature* 552:45. <https://doi.org/10.1038/nature24672>
- Cai W, Borlace S, Lengaigne M, van Rensch P, Collins M, Vecchi G, Timmermann A, Santoso A, McPhaden MJ, Wu L, England MH, Wang G, Guilyardi E, Jin F-F (2014) Increasing frequency of extreme El Niño events due to greenhouse warming. *Nature Clim Change* 4(2):111–116. <https://doi.org/10.1038/nclimate2100>
- Chen J, Bordoni S (2016) Early summer response of the East Asian summer monsoon to atmospheric CO₂ forcing and subsequent sea surface warming. *J Clim* 29(15):5431–5446. <https://doi.org/10.1175/JCLI-D-15-0649.1>
- Chen W, Lee J-Y, Ha K-J, Yun K-S, Lu R (2016) Intensification of the Western North Pacific anticyclone response to the short decaying El Niño event due to greenhouse warming. *J Clim* 29(10):3607–3627. <https://doi.org/10.1175/jcli-d-15-0195.1>
- Chen J, Wen Z, Wu R, Wang X, He C, Chen Z (2017) An interdecadal change in the intensity of interannual variability in summer rainfall over southern China around early 1990s. *Clim Dyn* 48(1):191–207. <https://doi.org/10.1007/s00382-016-3069-8>
- Chou C, Neelin JD, Chen C-A, Tu J-Y (2009) Evaluating the “Rich-Get-Richer” mechanism in tropical precipitation change under global warming. *J Clim* 22(8):1982–2005. <https://doi.org/10.1175/2008jcli2471.1>
- Chung CTY, Power SB (2016) Modelled impact of global warming on ENSO-driven precipitation changes in the tropical Pacific. *Clim Dyn* 47(3):1303–1323. <https://doi.org/10.1007/s00382-015-2902-9>
- Collins M, An S-I, Cai W, Ganachaud A, Guilyardi E, Jin F-F, Jochum M, Lengaigne M, Power S, Timmermann A, Vecchi G, Wittenberg A (2010) The impact of global warming on the tropical Pacific Ocean and El Niño. *Nature Geosci* 3(6):391–397
- Collins M, KachutaRao K, Ashok K, Bhandari S, Mitra AK, Prakash S, Srivastava R, Turner A (2013) Observational challenges in evaluating climate models. *Nat Clim Chang* 3:940–941
- Dai A, Wigley TML (2000) Global patterns of ENSO-induced precipitation. *Geophys Res Lett* 27(9):1283–1286. <https://doi.org/10.1029/1999gl1011140>
- Dee DP, Uppala SM, Simmons AJ et al (2011) The ERA-Interim reanalysis: configuration and performance of the data assimilation system. *Q J Roy Meteor Soc* 137(656):553–597. <https://doi.org/10.1002/qj.828>
- Ding YH (2007) The variability of the Asian summer monsoon. *J Meteorol Soc Jpn* 85B:21–54
- Deser C, Phillips A, Bourdette V, Teng H (2010) Uncertainty in climate change projections: the role of internal variability. *Clim Dynam* 38(3–4):527–546. <https://doi.org/10.1007/s00382-010-0977-x>
- Donat MG, Lowry AL, Alexander LV, O’Gorman PA, Maher N (2016) More extreme precipitation in the world’s dry and wet regions. *Nat Clim Chang* 6:508. <https://doi.org/10.1038/nclimate2941>
- Fan K, Xu Z, Tian B (2014) Has the intensity of the interannual variability in summer rainfall over South China remarkably increased? *Meteorol Atmos Phys* 124(1–2):23–32. <https://doi.org/10.1007/s00703-013-0301-5>
- Ferguson IM, Dracup JA, Duffy PB, Pegion P, Schubert S (2010) Influence of SST Forcing on Stochastic Characteristics of Simulated Precipitation and Drought. *J Hydrometeorol* 11(3):754–769. <https://doi.org/10.1175/2009jhm1132.1>
- Fischer EM, Rajczak J, Schär C (2012) Changes in European summer temperature variability revisited. *Geophys Res Lett* 39(19). doi:<https://doi.org/10.1029/2012GL052730>
- Fu Y (2012) The projected temporal evolution in the interannual variability of East Asian summer rainfall by CMIP3 coupled models. *Sci China Earth Sci* 56(8):1434–1446. <https://doi.org/10.1007/s11430-012-4430-3>
- Gleckler PJ, Taylor KE, Doutriaux C (2008) Performance metrics for climate models. *J Geophys Res: Atmos* 113(D6):D06104. <https://doi.org/10.1029/2007jd008972>
- Guan Z, Yamagata T (2003) The unusual summer of 1994 in East Asia: IOD teleconnections. *Geophys Res Lett*. <https://doi.org/10.1029/2002GL016831>

- Guo Y, Zhao Y, Wang J (2002) Numerical simulation of the relationships between the 1998 yangtze river valley floods and SST anomalies. *Adv Atmos Sci* 19(3):391–404. <https://doi.org/10.1007/s00376-002-0074-0>
- He J, Soden BJ (2017) A re-examination of the projected subtropical precipitation decline. *Nature Clim Change* 7(1):53–57. <https://doi.org/10.1038/nclimate3157>
- He C, Zhou T, Lin A, Wu B, Gu D, Li C, Zheng B (2015) Enhanced or weakened Western North Pacific subtropical high under global warming? *Sci Reports* 5:16771. <https://doi.org/10.1038/srep16771>
- He C, Lin A, Gu D, Li C, Zheng B (2017a) Formation mechanism for the amplitude of interannual climate variability in subtropical northern hemisphere: relative contributions from the zonal asymmetric mean state and the interannual variability of SST. *Clim Dyn* 48(1):697–705. <https://doi.org/10.1007/s00382-016-3105-8>
- He C, Wu B, Zou L, Zhou T (2017b) Responses of the summertime subtropical anticyclones to global warming. *J Clim* 30(16):6465–6479. <https://doi.org/10.1175/jcli-d-16-0529.1>
- Held IM, Soden BJ (2006) Robust responses of the hydrological cycle to global warming. *J Clim* 19(21):5686–5699. <https://doi.org/10.1175/jcli3990.1>
- Holmes CR, Woollings T, Hawkins E, de Vries H (2016) Robust future changes in temperature variability under greenhouse gas forcing and the relationship with thermal advection. *J Clim* 29(6):2221–2236. <https://doi.org/10.1175/jcli-d-14-00735.1>
- Hsu H-H, Liu X (2003) Relationship between the Tibetan Plateau heating and East Asian summer monsoon rainfall. *Geophys Res Lett*. <https://doi.org/10.1029/2003gl017909>
- Hu K, Huang G, Zheng X-T, Xie S-P, Qu X, Du Y, Liu L (2014) Interdecadal variations in ENSO influences on Northwest Pacific–East Asian early summertime climate simulated in CMIP5 models. *J Clim* 27(15):5982–5998. <https://doi.org/10.1175/jcli-d-13-00268.1>
- Hu X, Cai M, Yang S, Wu Z (2017) Delineation of thermodynamic and dynamic responses to sea surface temperature forcing associated with El Niño. *Clim Dyn*. <https://doi.org/10.1007/s00382-017-3711-0>
- Huang P, Xie S-P (2015) Mechanisms of change in ENSO-induced tropical Pacific rainfall variability in a warming climate. *Nature Geosci*. <https://doi.org/10.1038/ngeo2571>
- Huang Y, Li X, Wang H (2016) Will the western Pacific subtropical high constantly intensify in the future? *Clim Dyn* 47(1–2):567–577. <https://doi.org/10.1007/s00382-015-2856-y>
- Huang P, Chen D, Ying J (2017) Weakening of the tropical atmospheric circulation response to local sea surface temperature anomalies under global warming. *J Clim* 30(20):8149–8158. <https://doi.org/10.1175/jcli-d-17-0171.1>
- Kanamitsu M, Ebisuzaki W, Woollen J, Yang SK, Hnilo JJ, Fiorino M, Potter GL (2002) NCEP-DOE AMIP-II reanalysis (R-2). *Bull Am Meteorol Soc* 83(11):1631–1643. <https://doi.org/10.1175/bams-83-11-1631>
- Knutson TR, Manabe S (1995) Time-mean response over the tropical Pacific to increased CO₂ in a coupled Ocean–Atmosphere model. *J Clim* 8(9):2181–2199. [https://doi.org/10.1175/1520-0442\(1995\)008%3C2181:tmrott%3E2.0.co;2](https://doi.org/10.1175/1520-0442(1995)008%3C2181:tmrott%3E2.0.co;2)
- Knutson TR, McBride JL, Chan J, Emanuel K, Holland G, Landsea C, Held I, Kossin JP, Srivastava AK, Sugi M (2010) Tropical cyclones and climate change. *Nat Geosci* 3:157. <https://doi.org/10.1038/ngeo779>
- Kummu M, Gerten D, Heinke J, Konzmann M, Varis O (2014) Climate-driven interannual variability of water scarcity in food production potential: a global analysis. *Hydrol Earth Syst Sci* 18(2):447–461. <https://doi.org/10.5194/hess-18-447-2014>
- Lee D-K, Cha D-H, Kang H-S (2004) Regional climate simulation of the 1998 summer flood over East Asia. *J Meteorol Soc Jpn* 82(6):1735–1753. <https://doi.org/10.2151/jmsj.82.1735>
- Lee J-Y, Wang B, Seo K-H, Kug J-S, Choi Y-S, Kosaka Y, Ha K-J (2014) Future change of Northern hemisphere summer tropical–extratropical teleconnection in CMIP5 models. *J Clim* 27(10):3643–3664. <https://doi.org/10.1175/jcli-d-13-00261.1>
- Leonardo N, Hameed S (2015) Impact of the Hawaiian high on interannual variations of winter precipitation over California. *J Clim* 28(14):5667–5682. <https://doi.org/10.1175/jcli-d-14-00518.1>
- Li W, Li L, Ting M, Liu Y (2012) Intensification of Northern hemisphere subtropical highs in a warming climate. *Nat Geosci* 5(11):830–834. <https://doi.org/10.1038/ngeo1590>
- Li L, Li W, Barros AP (2013) Atmospheric moisture budget and its regulation of the summer precipitation variability over the Southeastern United States. *Clim Dyn* 41(3):613–631. <https://doi.org/10.1007/s00382-013-1697-9>
- Li T, Zhang L, Murakami H (2015) Strengthening of the Walker circulation under globalwarming in an aqua-planet general circulation model simulation. *Adv Atmos Sci* 32(11):1473–1480. <https://doi.org/10.1007/s00376-015-5033-7>
- Li G, Xie S-P, Du Y, Luo Y (2016) Effects of excessive equatorial cold tongue bias on the projections of tropical Pacific climate change. Part I: the warming pattern in CMIP5 multimodel ensemble. *Clim Dyn* 47(12):3817–3831. <https://doi.org/10.1007/s00382-016-3043-5>
- Li G, Xie S-P, He C, Chen Z (2017) Western Pacific emergent constraint lowers projected increase in Indian summer monsoon rainfall. *Nature Clim Change* 7(10):708–712. <https://doi.org/10.1038/nclimate3387>
- Lin R, Zhou T, Qian Y (2014) Evaluation of global monsoon precipitation changes based on five reanalysis datasets. *J Clim* 27(3):1271–1289. <https://doi.org/10.1175/jcli-d-13-00215.1>
- Liu YM, Wu GX, Ren RC (2004) Relationship between the subtropical anticyclone and diabatic heating. *J Clim* 17(4):682–698
- Liu R, Liu SC, Shiu C-J, Li J, Zhang Y (2016) Trends of regional precipitation and their control mechanisms during 1979–2013. *Adv Atmos Sci* 33(2):164–174. <https://doi.org/10.1007/s00376-015-5117-4>
- Long S-M, Xie S-P, Liu W (2016) Uncertainty in tropical rainfall projections: atmospheric circulation effect and the ocean coupling. *J Clim* 29(7):2671–2687. <https://doi.org/10.1175/JCLI-D-15-0601.1> doi
- Lu R, Fu Y (2010) Intensification of East Asian summer rainfall interannual variability in the twenty-first century simulated by 12 CMIP3 coupled models. *J Clim* 23(12):3316–3331. <https://doi.org/10.1175/2009jcli3130.1>
- Ma J, Xie S-P, Kosaka Y (2012) Mechanisms for tropical tropospheric circulation change in response to global warming. *J Clim* 25(8):2979–2994. <https://doi.org/10.1175/jcli-d-11-00048.1>
- Mearns LO, Rosenzweig C, Goldberg R (1992) Effect of changes in interannual climatic variability on CERES-wheat yields: sensitivity and 2 × CO₂ general circulation model studies. *Agric For Meteorol* 62(3):159–189. [https://doi.org/10.1016/0168-1923\(92\)90013-T](https://doi.org/10.1016/0168-1923(92)90013-T)
- Menon A, Levermann A, Schewe J (2013) Enhanced future variability during India’s rainy season. *Geophys Res Lett* 40(12):3242–3247. <https://doi.org/10.1002/grl.50583>
- Park C-K, Schubert SD (1997) On the nature of the 1994 East Asian summer drought. *J Clim* 10(5):1056–1070. [https://doi.org/10.1175/1520-0442\(1997\)010%3C1056:otnote%3E2.0.co;2](https://doi.org/10.1175/1520-0442(1997)010%3C1056:otnote%3E2.0.co;2)
- Park D-SR, Ho C-H, Chan JCL, Ha K-J, Kim H-S, Kim J, Kim J-H (2017) Asymmetric response of tropical cyclone activity to global warming over the North Atlantic and western North Pacific from CMIP5 model projections. *Sci Reports* 7:41354. <https://doi.org/10.1038/srep41354>
- Pendergrass AG, Gerber EP (2016) The rain is asked: two idealized models relating vertical velocity and precipitation distributions

- in a warming world. *J Clim* 29(18):6445–6462. <https://doi.org/10.1175/jcli-d-16-0097.1>
- Pendergrass AG, Knutti R, Lehner F, Deser C, Sanderson BM (2017) Precipitation variability increases in a warmer climate. *Sci Reports* 7(1):17966. <https://doi.org/10.1038/s41598-017-17966-y>
- Perkins-Kirkpatrick SE, Gibson PB (2017) Changes in regional heat-wave characteristics as a function of increasing global temperature. *Sci Reports* 7(1):12256. <https://doi.org/10.1038/s41598-017-12520-2>
- Pfahl S, O’Gorman PA, Fischer EM (2017) Understanding the regional pattern of projected future changes in extreme precipitation. *Nat Clim Chang* 7:423. <https://doi.org/10.1038/nclimate3287>
- Power SB, Delage F, Colman R, Moise A (2012) Consensus on twenty-first-century rainfall projections in climate models more widespread than previously thought. *J Clim* 25(11):3792–3809. <https://doi.org/10.1175/jcli-d-11-00354.1>
- Qu X, Huang G (2016) The global warming-induced South Asian high change and its uncertainty. *J Clim* 29(6):2259–2273. <https://doi.org/10.1175/JCLI-D-15-0638.1> doi
- Rodwell MJ, Hoskins BJ (2001) Subtropical anticyclones and summer monsoons. *J Clim* 14(15):3192–3211. [https://doi.org/10.1175/1520-0442\(2001\)014%3C3192:saasm%3E2.0.co;2](https://doi.org/10.1175/1520-0442(2001)014%3C3192:saasm%3E2.0.co;2)
- Schneider T, O’Gorman PA, Levine XJ (2010) Water Vapor and the dynamics of climate changes. *Rev Geophys* 48(3):RG3001. <https://doi.org/10.1029/2009rg000302>
- Seager R, Naik N, Vecchi GA (2010) Thermodynamic and dynamic mechanisms for large-scale changes in the hydrological cycle in response to global warming. *J Clim* 23(17):4651–4668. <https://doi.org/10.1175/2010jcli3655.1>
- Seager R, Naik N, Vogel L (2012) Does global warming cause intensified interannual hydroclimate variability? *J Clim* 25(9):3355–3372. <https://doi.org/10.1175/jcli-d-11-00363.1>
- Simon Wang SY, Huang W-R, Hsu H-H, Gillies RR (2015) Role of the strengthened El Niño teleconnection in the May 2015 floods over the southern Great Plains. *Geophys Res Lett* 42(19):8140–8146. <https://doi.org/10.1002/2015gl065211>
- Sohn B-J, Lee S, Chung E-S, Song H-J (2016) The role of the dry static stability for the recent change in the Pacific walker circulation. *J Clim* 29(8):2765–2779. <https://doi.org/10.1175/JCLI-D-15-0374.1> doi
- Stevenson S, Fox-Kemper B, Jochum M, Neale R, Deser C, Meehl G (2012) Will there be a significant change to El Niño in the twenty-first century? *J Clim* 25(6):2129–2145. <https://doi.org/10.1175/jcli-d-11-00252.11>
- Stevenson S, Timmermann A, Chikamoto Y, Langford S, DiNezio P (2015) Stochastically generated North American Megadroughts. *J Clim* 28(5):1865–1880. <https://doi.org/10.1175/jcli-d-13-00689.1>
- Sun Y, Zhang X, Zwiers FW, Song L, Wan H, Hu T, Yin H, Ren G (2014) Rapid increase in the risk of extreme summer heat in Eastern China. *Nature Clim Change* 4(12):1082–1085. <https://doi.org/10.1038/nclimate2410>
- Tao W, Huang G, Hu K, Qu X, Wen G, Gong H (2015) Interdecadal modulation of ENSO teleconnections to the Indian Ocean Basin Mode and their relationship under global warming in CMIP5 models. *Int J Climatol* 35(3):391–407. <https://doi.org/10.1002/joc.3987>
- Taylor KE, Stouffer RJ, Meehl GA (2012) An overview of CMIP5 and the experiment design. *Bull Am Meteorol Soc* 93(4):485–498. <https://doi.org/10.1175/bams-d-11-00094.1>
- Trenberth KE, Dai A, Rasmussen RM, Parsons DB (2003) The changing character of precipitation. *Bull Am Meteorol Soc* 84(9):1205–1217. <https://doi.org/10.1175/bams-84-9-1205>
- Vuuren D, Edmonds J, Kainuma M et al (2011) The representative concentration pathways: an overview. *Clim Change* 109(1–2):5–31. <https://doi.org/10.1007/s10584-011-0148-z>
- Wallace JM, Rasmusson EM, Mitchell TP, Kousky VE, Sarachik ES, Von Storch H (1998) On the structure and evolution of ENSO-related climate variability in the tropical Pacific: Lessons from TOGA. *J Geophys Res Oceans* 103(C7):14241–14259. <https://doi.org/10.1029/97JC02905>
- Wang Z, Duan A, Yang S, Ullah K (2017a) Atmospheric moisture budget and its regulation on the variability of summer precipitation over the Tibetan Plateau. *J Geophys Res: Atmos* 122(2):614–630. <https://doi.org/10.1002/2016jd025515>
- Wang X, Jiang D, Lang X (2017b) Future extreme climate changes linked to global warming intensity. *Sci Bull* 62(24):1673. <https://doi.org/10.1016/j.scib.2017.11.004> doi
- Watanabe M, Kamae Y, Kimoto M (2014) Robust increase of the equatorial Pacific rainfall and its variability in a warmed climate. *Geophys Res Lett* 41(9):2014GL059692. <https://doi.org/10.1002/2014gl059692>
- Wei W, Zhang R, Wen M, Rong X, Li T (2014) Impact of Indian summer monsoon on the South Asian High and its influence on summer rainfall over China. *Clim Dyn* 43(5–6):1257–1269. <https://doi.org/10.1007/s00382-013-1938-y>
- Wen N, Liu Z, Liu Y (2015) Direct impact of El Niño on East Asian summer precipitation in the observation. *Clim Dyn* 44(11–12):2979–2987. <https://doi.org/10.1007/s00382-015-2605-2>
- Wu B, Zhou T, Li T (2017) Atmospheric dynamic and thermodynamic processes driving the Western North Pacific anomalous anticyclone during El Niño. Part I: maintenance mechanisms. *J Clim* 30(23):9621–9635. <https://doi.org/10.1175/jcli-d-16-0489.1>
- Xie PP, Arkin PA (1997) Global precipitation: A 17-year monthly analysis based on gauge observations, satellite estimates, and numerical model outputs. *Bull Am Meteorol Soc* 78(11):2539–2558. [https://doi.org/10.1175/1520-0477\(1997\)078%3C2539:gpayma%3E2.0.co;2](https://doi.org/10.1175/1520-0477(1997)078%3C2539:gpayma%3E2.0.co;2)
- Yanai M, Tomita T (1998) Seasonal and interannual variability of atmospheric heat sources and moisture sinks as determined from NCEP-NCAR reanalysis. *J Clim* 11(3):463–482
- Yin X, Gruber A, Arkin P (2004) Comparison of the GPCP and CMAP merged Gauge–Satellite monthly precipitation products for the period 1979–2001. *J Hydrometeorol* 5(6):1207–1222. <https://doi.org/10.1175/jhm-392.1>
- Yoon J-H, Wang SYS, Gillies RR, Kravitz B, Hipps L, Rasch PJ (2015) Increasing water cycle extremes in California and in relation to ENSO cycle under global warming. *Nat Commun* 6:8657. <https://doi.org/10.1038/ncomms9657>
- Zhang L, Li T (2014) A simple analytical model for understanding the formation of sea surface temperature patterns under global warming. *J Clim* 27(22):8413–8421. <https://doi.org/10.1175/jcli-d-14-00346.1>
- Zhang L, Li T (2017) Relative roles of differential SST warming, uniform SST warming and land surface warming in determining the Walker circulation changes under global warming. *Clim Dyn* 48(3):987–997. <https://doi.org/10.1007/s00382-016-3123-6>
- Zhang L, Zhou T (2015) Drought over East Asia: a review. *J Clim* 28(8):3375–3399. <https://doi.org/10.1175/jcli-d-14-00259.1>
- Zhang P, Liu Y, He B (2016) Impact of East Asian summer monsoon heating on the interannual variation of the South Asian High. *J Clim* 29(1):159–173. <https://doi.org/10.1175/jcli-d-15-0118.1>